



A pointwise weighting prediction variance–high-dimensional model representation model-based global optimization approach for ship hull parametric design

Zhijian Zha, Baoping Li, Xiaokui Zhou, Chu Wang, Qi Zhou & Jiexiang Hu

To cite this article: Zhijian Zha, Baoping Li, Xiaokui Zhou, Chu Wang, Qi Zhou & Jiexiang Hu (20 Aug 2024): A pointwise weighting prediction variance–high-dimensional model representation model-based global optimization approach for ship hull parametric design, Engineering Optimization, DOI: [10.1080/0305215X.2024.2388642](https://doi.org/10.1080/0305215X.2024.2388642)

To link to this article: <https://doi.org/10.1080/0305215X.2024.2388642>

 View supplementary material 

 Published online: 20 Aug 2024.

 Submit your article to this journal 

 Article views: 68

 View related articles 

 View Crossmark data 



A pointwise weighting prediction variance–high-dimensional model representation model-based global optimization approach for ship hull parametric design

Zhijian Zha^{a,b}, Baoping Li^a, Xiaokui Zhou^c, Chu Wang^a, Qi Zhou^{a,b} and Jiexiang Hu^a

^aSchool of Aerospace Engineering, Huazhong University of Science & Technology, Wuhan, People's Republic of China; ^bShanghai Key Laboratory of Ship Engineering, Shanghai, People's Republic of China; ^cMarine Design and Research Institute of China, Shanghai, People's Republic of China

ABSTRACT

Ship hull optimization techniques based on computer-aided design/computational fluid dynamics can effectively enhance the efficiency and stability of ship designs, with significant application prospects. To enhance the potential of ship hull optimization, increasing design variable dimensionality is essential, but can cause a significant increase in hydrodynamic simulations. To reduce simulations required for high-dimensional ship hull optimization, a new surrogate method, pointwise weighting prediction variance–high-dimensional model representation (PWPV-HDMR), which uses pointwise weighting prediction variance (PWPV) to aggregate different *a priori* assumptions, is developed. Moreover, a differential evolution algorithm is used to identify promising hull design parameters, using the PWPV-HDMR model instead of costly simulation as the fitness function. The proposed approach is tested on the hydrostatic resistance optimization of KRISO Container Ship. The results show that PWPV-HDMR outperforms kriging-HDMR, with a better resistance optimization effect, illustrating the effectiveness of the PWPV-HDMR-based global optimization approach in discovering promising ship hull parameters.

ARTICLE HISTORY

Received 9 March 2024

Accepted 31 July 2024

KEYWORDS

High-dimensional model representation; surrogate modelling; free-form deformation; hull form optimization

1. Introduction

The study of low-resistance design optimization for ships can effectively improve the efficiency of ship operation, thereby reducing energy consumption and minimizing pollution. Traditional ship design optimization typically involves modifying the moulded lines of the mother ship based on a series of ship model test data (Maruo *et al.* 1977). This process is often cumbersome, requiring continuous experimental validation, resulting in high costs, long cycles and limited improvement effects. With advances in numerical methods and computer performance, numerical simulation has become a predictive means for hydrodynamic performance, accelerating the research on low-resistance design optimization for ships. This has led to the emergence of a new model for ship design optimization based on computer-aided design and computational fluid dynamics (CAD/CFD) (Choo *et al.* 2020; Nazemian and Ghadimi 2021). As shown in Figure 1, the design optimization provides parameterized variables for the modelling-simulation process, while the modelling-simulation process provides objective and constraint functions for the design optimization.

CONTACT Jiexiang Hu  jiexianghuhust@gmail.com

 Supplemental data for this article can be accessed online at <https://doi.org/10.1080/0305215X.2024.2388642>.

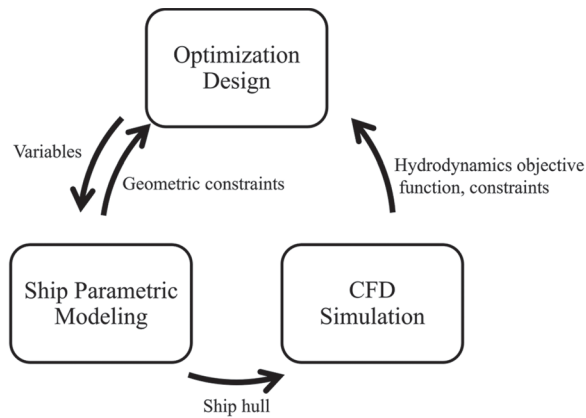


Figure 1. Ship design optimization model based on computer-aided design/computational fluid dynamics (CAD/CFD).

The geometric parameterization and reconstruction of the ship hull are the primary steps in ship design optimization based on the CAD/CFD model. Various curve and surface modelling methods have been proposed, including free-form deformation (FFD) (S. Li *et al.* 2022), parameterized non-uniform rational B-splines (NURBS) (H. Zhou *et al.* 2022), geometric blending (Evans *et al.* 2015), surface perturbation (Peri, Rossetti, and Campana 2001) and shifting methods (S. Li *et al.* 2022). In this article, FFD technology is used for the parametric expression and reconstruction of the ship's hull shape. This choice is attributed to the ability of FFD technology to facilitate global or local deformation of the ship's shape by adjusting the control volume, thereby providing a convenient means to explore more possibilities for the hull shape.

During the design optimization of the ship hull, to enhance the optimization potential, it is necessary to appropriately increase the dimensionality and variation range of design variables. However, as the dimensionality increases, the number of required ship hydrodynamic simulations rises sharply, rendering the design optimization impractical. Constructing surrogate models to fit the relationship between inputs and outputs as an alternative to time-consuming CFD simulations has become an effective approach to address these challenges (Diez *et al.* 2019; Feng *et al.* 2018; F. Huang, Wang, and Yang 2016; Jeong and Kim 2013; Lin *et al.* 2021; Wei *et al.*, "Sensitivity Analysis," 2019; Q. Zhou *et al.* 2017). For example, Wan *et al.* (2022) used a fourth-order polynomial response surface (PRS) model in the integrated design of the hull form for underwater surface vessels to establish a surrogate model for hydrodynamic performance. Kim *et al.* (2011) used the kriging surrogate model to fit the relationship between the hull form parameters of the 60 series and wave resistance within a specified speed range. Tian *et al.* (2021) used the radial basis function (RBF) model to establish the relationship between nine design parameters of the medical semi-submersible platform and the hull structural weight, heave response and roll response of the hull. Wei *et al.* ("Hull Form," 2019) used the polynomial chaos expansion (PCE) model to establish the relationship between the bow shape parameters of the KRISO Container Ship (KCS) model and the ship energy efficiency design index (EEDI). Feng *et al.* (2018) used the support vector regression (SVR) model to construct the relationship between the hull parameters of an offshore aquaculture vessel and the resistance and the circumferential non-uniformity of the wave field. However, existing research on ship hull parameters design has primarily used surrogate modelling methods to address lower-dimensional optimization problems, finding optimal solutions in local regions. Meanwhile, traditional surrogate models used in ship hull form optimization still face challenges of low modelling accuracy and high computational costs in high-dimensional spaces.

To overcome these limitations, this article proposes a global optimization approach based on a high-dimensional surrogate model using the Cut-HDMR framework, referred to as pointwise

weighting prediction variance–high-dimensional model representation (PWPV-HDMMR). The Cut-HDMMR framework is a common solution for high-dimensional problems (Chen *et al.* 2019; Rabitz and Aliş 1999; Sobol' 2003; Zhang, Qiao, and Wu 2024). Preliminary research suggests that using different traditional surrogate models to construct the basis functions of the Cut-HDMMR framework can have a significant impact on the predictive performance of the final model (Chen *et al.* 2019; Luo, Li, and Wang 2021; Sobol' 2003; Zhang *et al.* 2022). Specially, because of the black-box nature of the relationship between ship hull parameters and hydrodynamic performance, and the costly nature of acquiring information that describes the relationship between the two, engineers often find it challenging to determine which traditional surrogate model is the optimal choice for constructing the basis functions of the Cut-HDMMR framework (Z. Huang *et al.* 2015; Shan and Wang 2009; H. Wang, Tang, and Li 2011). Furthermore, considering that many researchers have mentioned that a more accurate surrogate model can be obtained by combining multiple surrogate models (Ren *et al.* 2022; L. Wang *et al.* 2021; X. Wang *et al.* 2023), these methods are rarely applied to address high-dimensional problems in these studies. Therefore, the proposed method aggregates three traditional surrogates to reduce the risk of using inappropriate surrogate models during the construction of the basis function. To calculate the weighting coefficients of these surrogate models, the true responses at nearby sample points are used to estimate the prediction variance at non-sampling points. Moreover, the differential evolution (DE) algorithm is used to identify promising hull design parameters, where the fitness values assigned to the population are provided by the constructed PWPV-HDMMR. The effectiveness of the promising ship hull parameters thus obtained is validated through simulation experiments of KCS static water towing.

The remaining sections of this article are organized as follows. Section 2 provides a detailed description of the PWPV-HDMMR method. Section 3 compares the predictive performance of PWPV-HDMMR and individual Cut-HDMMR models. Section 4 details the parameterization methods and simulation settings for KCS static water towing resistance. Section 5 explores promising ship hull parameters and validates their consistency with simulation results. Finally, Section 6 concludes the article.

2. Pointwise weighted combination high-dimensional surrogate model based on prediction variance: PWPV-HDMMR

2.1. High-dimensional model representation (HDMMR)

The HDMMR method decomposes high-dimensional problems into a series of lower-dimensional problems to be solved. Its general form is expressed as follows (Chen *et al.* 2019):

$$f(X) = f_0 + \sum_{i=1}^d f_i(x_i) + \sum_{1 \leq i < j \leq d} f_{ij}(x_i, x_j) + \sum_{1 \leq i < j < k \leq d} f_{ijk}(x_i, x_j, x_k) + \dots$$

$$\sum_{1 \leq i < j < \dots < r \leq d} f_{ij\dots r}(x_i, x_j, \dots, x_r) + \dots + f_{12\dots d}(x_1, x_2, \dots, x_d) \quad (1)$$

where the d -dimensional vector $X = [x_1, x_2, \dots, x_d]^T \in R^d$ represents the input variables of the model; $f(X)$ is the output value of the high-dimensional function; f_0 is the constant term, known as the zero-order function; $f_i(x_i)$ indicates the contribution to the output when only variable x_i is active, known as the first-order basis function; $f_{ij}(x_i, x_j)$ represents the contribution to the output when variables x_i and x_j are coupled, known as the second-order basis function; and $f_{12\dots d}(x_1, x_2, \dots, x_d)$ represents the contribution to the output when all variables act together.

Cut-HDMMR decomposes the original function into the sum of functions on cutting lines, cutting planes and cutting hyperplanes passing through a given point $\mathbf{x}_0 = (x_1^0, x_2^0, \dots, x_d^0)$ is typically chosen at the centre of the design space and is commonly referred to as the 'cutting centre'

of the high-dimensional model. The expressions for the various-order functions in Cut-HDMR are as follows (Chen *et al.* 2019):

$$f_0 = f(\mathbf{x}_0) \quad (2)$$

$$f_i(x_i) = f(x_i, \mathbf{x}_0^i) - f_0 \quad (3)$$

$$f_{ij}(x_i, x_j) = f(x_i, x_j, \mathbf{x}_0^{ij}) - f_i(x_i) - f_j(x_j) - f_0 \quad (4)$$

$$\begin{aligned} f_{ijk}(x_i, x_j, x_k) &= f(x_i, x_j, x_k, \mathbf{x}_0^{ijk}) - f_{ij}(x_i, x_j) - f_{ik}(x_i, x_k) \\ &\quad - f_{jk}(x_j, x_k) - f_i(x_i) - f_j(x_j) - f_k(x_k) - f_0 \end{aligned} \quad (5)$$

⋮

$$f_{1\dots d}(x_1, \dots, x_d) = f(\mathbf{x}) - f_0 - \sum_i f_i(x_i) - \sum_{ij} f_{ij}(x_i, x_j) - \dots \quad (6)$$

where f_0 is the response value of point \mathbf{x}_0 ; \mathbf{x}_0^i represents the cutting centre point vector without the i th dimension; and \mathbf{x}_0^{ij} indicates the cutting centre point vector without dimensions i, j . Each first-order basis function $f_i(x_i)$ can be obtained along the x_i -axis passing through the centre point \mathbf{x}_0 , and each second-order basis function $f_{ij}(x_i, x_j)$ can be obtained on the plane passing through the centre point \mathbf{x}_0 and x_i, x_j axes. For a complex system, higher-order couplings between variables are often relatively small in practice (Liu *et al.* 2018). Therefore, when using Cut-HDMR, the higher-order basis functions in equations are generally negligible.

The preliminary research suggests that using different traditional surrogate models to construct the basis functions of the HDMR framework can have a significant impact on the predictive performance of the final model (Z. Huang *et al.* 2015; Shan and Wang 2009; H. Wang, Tang, and Li 2011). However, the challenge arises in selecting the most suitable surrogate model, owing to a shortage of adequate prior information describing the relationship between inputs and outputs. Therefore, instead of selecting a traditional surrogate arbitrarily to construct basis functions, this article proposes a method to aggregate multiple surrogate models, to leverage the strengths of each model.

2.2. Pointwise weighted prediction variance–high-dimensional surrogate model (PWPV-HDMR)

To construct promising basis functions of PWPV-HDMR, three traditional surrogate models are used. The PRS surrogate model is characterized by its simple construction and high accuracy in linear fitting. The kriging surrogate model excels in both global and local fitting accuracy. The SVR surrogate model is adept at handling nonlinear problems and exhibits good generalization capabilities. In this study, the basis functions of PWPV-HDMR are constructed using a weighted average of these three sub-surrogate models. It is expressed as follows:

$$\begin{aligned} \hat{f}(X) &= f_0 + \sum_{i=1}^d \hat{f}_i(x_i) + \sum_{1 \leq i < j \leq d} \hat{f}_{ij}(x_i, x_j) \\ &= f_0 + \sum_{i=1}^d \sum_{t=1}^M w_{ij}^t \hat{f}_i^t(x_i) + \sum_{1 \leq i < j \leq d} \sum_{t=1}^M w_{ij}^t \hat{f}_{ij}^t(x_i, x_j) \end{aligned} \quad (7)$$

where t represents the t th sub-surrogate model, and w_i^t is the weighting coefficient, representing the relative contribution rate of each sub-surrogate model. To satisfy the unbiased condition, it is required that the sum of these weighting coefficients equals 1.

An assumption used to calculate the weighting coefficient is that if a sub-surrogate model has less prediction variance at a certain location, its weighting coefficient should be larger, and if its predicted value deviates further from the true response, its weighting coefficient should be smaller. Since each sub-surrogate model approaches the true response to different extents in different regions, their weighting coefficients need to be calculated with reference to position to achieve better modelling accuracy. Moreover, considering that the true responses at non-sampling points are unknown, the responses of nearby sample points are used as an estimation. Based on this assumption, the prediction variance $\sigma_t^2(\hat{x})$ of the t th sub-surrogate model $\hat{f}_t(x)$ at non-sampling point \hat{x} can be expressed as:

$$\sigma_t^2(\hat{x}) = \frac{1}{\nu} \sum_{h=1}^{\nu} [(y(x_h) - \hat{y}_t(x_h))]^2 \quad (8)$$

where $p_1 = \{x_1, x_2, \dots, x_\nu\}$ denotes the ν nearest sample points to the non-sampling point \hat{x} , $\{y(x_1), y(x_2), \dots, y(x_\nu)\}$ is the true response values of these ν sample points, and $\{\hat{y}'_t(x_1), \hat{y}'_t(x_2), \dots, \hat{y}'_t(x_\nu)\}$ comprises values predicted by the validation surrogate model $\hat{f}'_t(x)$ of the t th sub-surrogate model $\hat{f}_t(x)$ at these ν sample points. The sample points in p_1 are selected through the following conditions:

$$D = \{\|\hat{x} - x_i\| \mid x_i \in N\} \quad (9)$$

$$p_1 = \{x_i \mid \|\hat{x} - x_i\| \in \min_\nu(D) \text{ and } x_i \in N\} \quad (10)$$

where $N = \{x_1, x_2, \dots, x_n\}$ is the training set used to construct sub-surrogate models $\hat{f}_t(x)$, and $p_2 = \{x_i \mid x_i \notin p_1 \text{ and } x_i \in N\}$ is used to construct the validation surrogate models $\hat{f}'_t(x)$ of the sub-surrogate models $\hat{f}_t(x)$. The value of ν is empirically chosen. Considering that each basis function uses a small number of sample points, ν is typically selected as 1 or 2. In this article, the following formulae were used to choose the ν value:

$$\begin{cases} \nu = 2, & D_3^* - D_2^* \geq D_2^* - D_1^* \\ \nu = 1, & D_3^* - D_2^* < D_2^* - D_1^* \end{cases} \quad (11)$$

where D_n^* is the Euclidean distance between the n th closest sample points and the non-sampling point \hat{x} . $D_3^* - D_2^* \geq D_2^* - D_1^*$ means that D_2^* is closer to D_1^* than D_3^* , and both the first and second closest sample points were used to estimate the non-sampling point \hat{x} . $D_3^* - D_2^* < D_2^* - D_1^*$ means that D_2^* is closer to D_3^* than D_1^* , and only the closest sample points were used to estimate the non-sampling point \hat{x} .

Based on the above assumptions and formulae, the calculation of the pointwise weighting coefficient is expressed as follows:

$$w_t(\hat{x}) = \frac{\frac{1}{\sigma_t^2(\hat{x})}}{\sum_{i=1}^M \frac{1}{\sigma_i^2(\hat{x})}} \quad (12)$$

where M is the number of sub-surrogate models in the ensemble model. After calculating the weighting coefficients $w_t(x)$ of all sub-surrogate models at the non-sampling point \hat{x} , the predicted value at point \hat{x} can be expressed as:

$$\hat{y}_e(\hat{x}) = \sum_{t=1}^M w_t(\hat{x}) \hat{f}_t(\hat{x}) \quad (13)$$

The specific modelling process of PWPV-HDMR is illustrated in Figure 2, and the detailed steps are implemented as follows.

- **Step 1.** Generation of cutting centre point \mathbf{x}_0 : Select the centre point $\mathbf{x}_0 = (x_1^0, x_2^0, \dots, x_d^0)$ of the design space as the cutting centre point for Cut-HDMR and evaluate the corresponding response value f_0 .
- **Step 2.** Construction of first-order approximation basis function $\hat{f}_i(x_i)$: First, obtain the boundary points x_i^U, x_i^L on the axis x_i and evaluate the corresponding response values $f_i(x_i^U, x_0^i), f_i(x_i^L, x_0^i)$. Then, check the linearity of the first-order approximation function. If $\left\| \frac{f_i(x_i^U, x_0^i) - f_i(x_i^L, x_0^i)}{x_i^U - x_i^L} (x_i^0 - x_i^L) + f_i(x_i^L) - f_i(x_0) \right\| / \|f_i(x_0)\|$ is less than ε_1 , where ε_1 is a small threshold used to determine the nonlinearity of the function, $f_i(x_i)$ is considered to be linear. In this case, a linear regression model $\hat{f}_i(x_i) = ax_i + b$ is established using the existing sample points. Otherwise, construct the first-order approximation function $\hat{f}_i(x_i) = \sum_{t=1}^M w_{it}^t \hat{f}_i^t(x_i)$ through the Diving RECTangles (DIRECT) adaptive sampling method, and assess the convergence of $\hat{f}_i(x_i)$. If it converges, stop the modelling process for this basis function and proceed to the next step. Otherwise, perform sequential sampling and modelling until the constructed i th approximation function $\hat{f}_i(x_i)$ converges.
- **Step 3.** Construction of remaining first-order approximation basis function $\hat{f}_j(x_j)$: Repeat Step 2 to construct surrogate models for all remaining first-order basis functions. At this point, the first-order part of the model has been constructed.
- **Step 4.** Determination of whether the second-order part of the model exists: Calculate the response values $f(\mathbf{x}^U)$ and $f(\mathbf{x}^L)$ at the upper and lower bounds \mathbf{x}^U and \mathbf{x}^L of the design space. If both $\left\| \left[f_0 + \sum_i^d \hat{f}_i(x_i^U) - f(x^U) \right] / f(x^U) \right\|$ and $\left\| \left[f_0 + \sum_i^d \hat{f}_i(x_i^L) - f(x^L) \right] / f(x^L) \right\|$ are less than ε_2 , where the typical value for ε_2 is often 0.1, then the second-order part does not exist, and the model construction is complete. Otherwise, proceed to Step 5.
- **Step 5.** Determination and construction of second-order approximation basis function $\hat{f}_{i,j}(x_i, x_j)$: First, select a second-order sample point (x_i, x_j, x_0^{ij}) and evaluate the corresponding response value $f(x_i, x_j, x_0^{ij})$. If the value of $f_0 + \hat{f}_i(x_i) + \hat{f}_j(x_j)$ is close to $f(x_i, x_j, x_0^{ij})$, then $f_{i,j}(x_i, x_j)$ is considered not to exist, and modelling for it is halted. Otherwise, using \mathbf{x}_0 and the sample points collected during the construction of first-order basis functions $\hat{f}_i(x_i)$ and $\hat{f}_j(x_j)$ as initial sample points, employ the DIRECT adaptive sampling method to construct the corresponding second-order approximation basis function $\hat{f}_{i,j}(x_i, x_j) = \sum_{t=1}^M w_{ijt}^t \hat{f}_{ij}^t(x_i, x_j)$ until convergence.
- **Step 6.** Construction of remaining second-order approximation basis function $\hat{f}_{k,l}(x_k, x_l)$: Repeat Step 5 to construct surrogate models for all remaining second-order basis functions. Finally, combine the first-order and second-order basis functions with the response value at the centre cutting point, and the resulting model is the desired PWPV-HDMR model.

3. Numerical study

3.1. Analysis of case results

In this study, 15 numerical test cases were used to assess the performance of the PWPV-HDMR model across different dimensionalities, as outlined in Tables A1–A4 in Appendix A. The evaluation includes a comparison with three individual cut-HDMR models, *i.e.* kriging-HDMR (Ji *et al.* 2022), PRS-HDMR (Zhao 2018) and SVR-HDMR (G. Li *et al.* 2017), as well as the kriging model. In the subsequent discussion, the term basic HDMRs refers to the kriging-HDMR, PRS-HDMR and SVR-HDMR models. For each model, to conduct a more comprehensive evaluation and a more robust

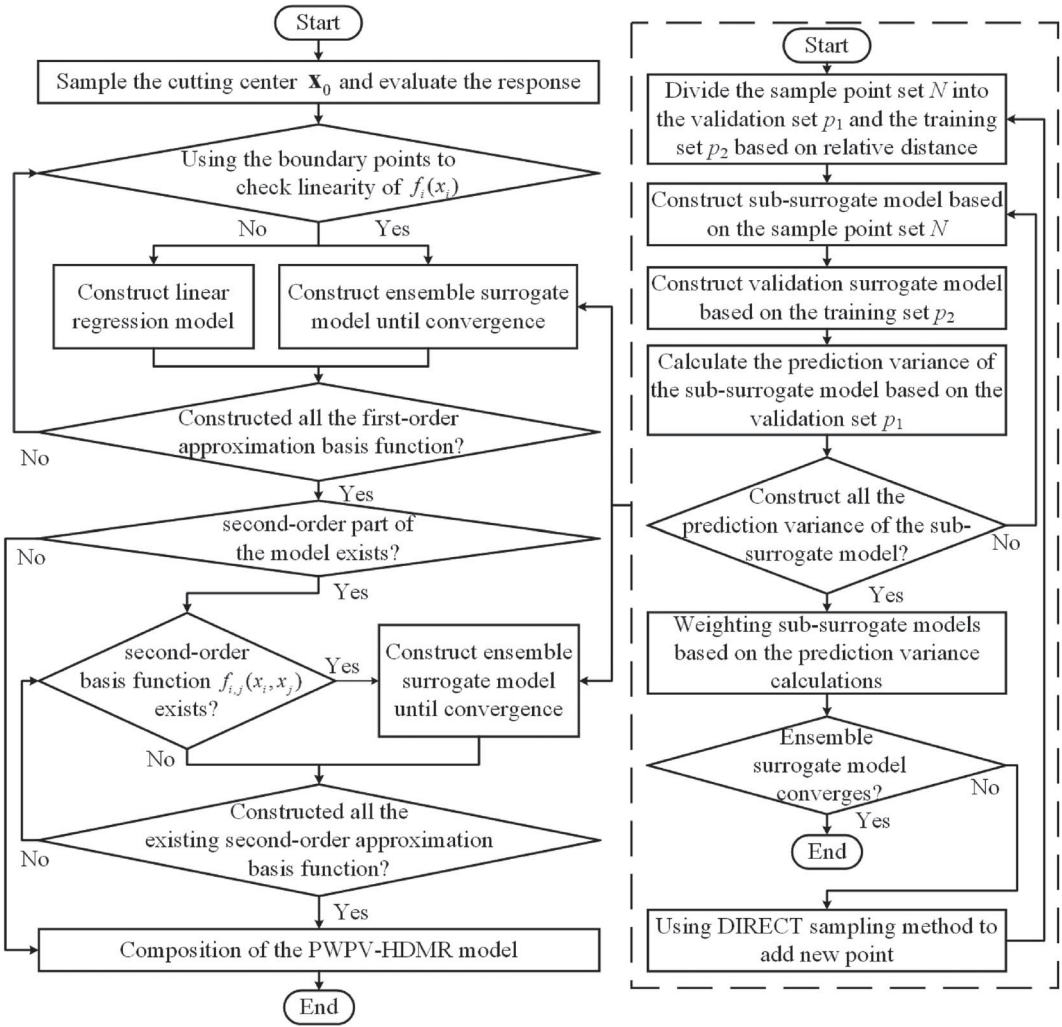


Figure 2. Flowchart of the pointwise weighting prediction variance–high-dimensional model representation (PWPV-HDMR) model. DIRECT = Dividing RECTangles.

significance analysis, 1000 validation points were used to assess the predictive performance through four error metrics: the coefficient of determination (R^2), relative root mean square error (RRMSE), relative maximum absolute error (RMAE) and relative average absolute error (RAAE). The expression for the relative improvement of the PWPV-HDMR model compared to other models is as follows:

$$Relative\ improvement_{other} = \left(1 - \frac{err_{PWPV-HDMR}}{err_{other}}\right) \times 100\% \quad (14)$$

where $err(\cdot)$ is one of the four error metrics mentioned above, and the subscript 'other' represents the four surrogate models other than the PWPV-HDMR model. In addition, the number of sample points used in constructing the model is recorded as 'NOP', with the number following the plus sign indicating the sample points used to validate or construct second-order components of the Cut-HDMR models. Both PWPV-HDMR and basic HDMR models use the DIRECT adaptive sampling method to obtain new points. Sampling stops when the relative error between the predicted and true values of new points is less than 1%. The sample points used to construct the kriging model are obtained

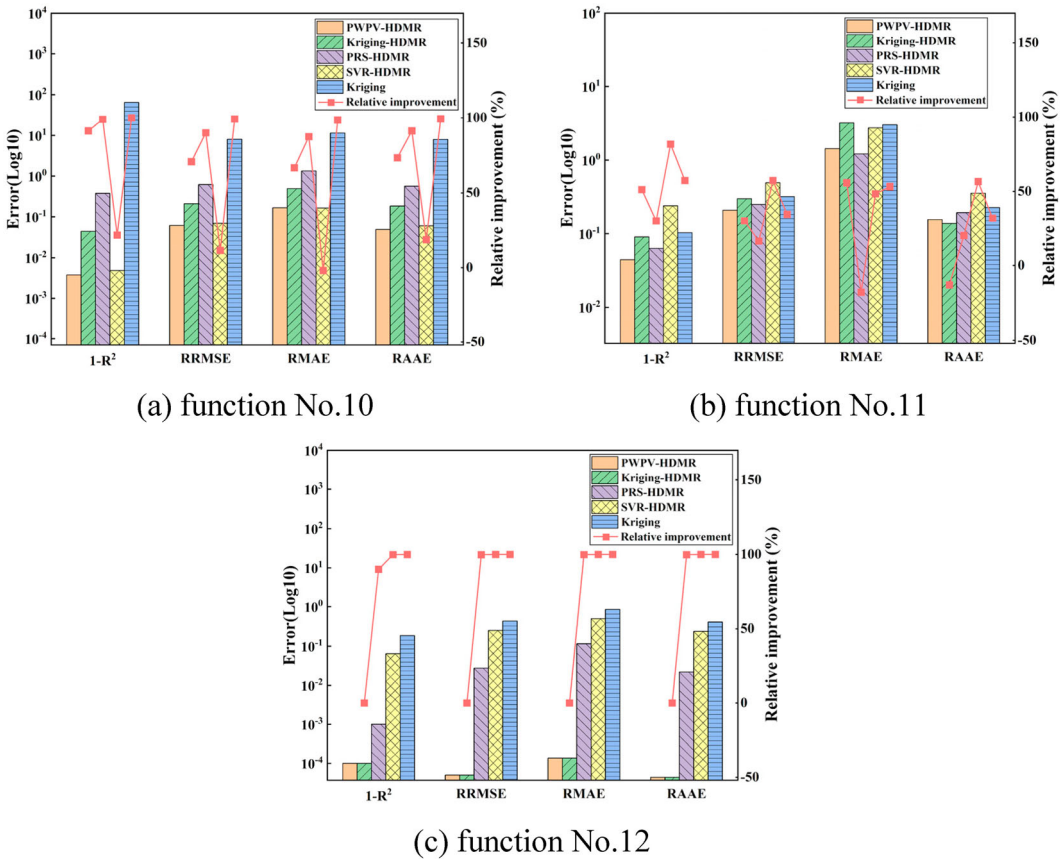


Figure 3. Modelling accuracy and relative improvement of the pointwise weighting prediction variance–high-dimensional model representation (PWPV-HDMR) (30 dimensions): (a) function no. 10; (b) function no. 11; (c) function no. 12. HDMR = high-dimensional model representation; PRS = polynomial response surface; SVR = support vector regression; R^2 = coefficient of determination; RRMSE = relative root mean square error; RMAE = relative maximum absolute error; RAAE = relative average absolute error.

through the optimized Latin hypercube method, with the same number as the HDMR models. Tables 1 and 2 show the modelling accuracy results for 30 and 40 dimensions, while a more intuitive analysis of the comparative results is demonstrated in Figures 3 and 4.

From the histogram in Figure 3, it can be observed that the modelling accuracy of the PWPV-HDMR model is the best in cases 10 and 11, while the results of the kriging model are consistently the worst in cases 10 and 12. Among the three basic HDMR models, kriging-HDMR performs the best in case 12, PRS-HDMR excels in case 11 and SVR-HDMR performs the best in case 10. This indicates that these three models have their strengths and weaknesses, justifying the significance of composing a combined surrogate model.

The line chart in Figure 3 represents the improvement percentage of the PWPV-HDMR model relative to the other four models. It can be observed that: (1) In case 12, the SVR-HDMR model and the PWPV-HDMR model perform the best, with significantly higher accuracy than the other two basic HDMR models, which means that the PWPV-HDMR model clearly learns the characteristics of SVR-HDMR, achieving better results than the other models. (2) In cases 10 and 11, when the differences in accuracy among the three basic HDMR models are relatively small, the PWPV-HDMR model achieves optimal predictive results.

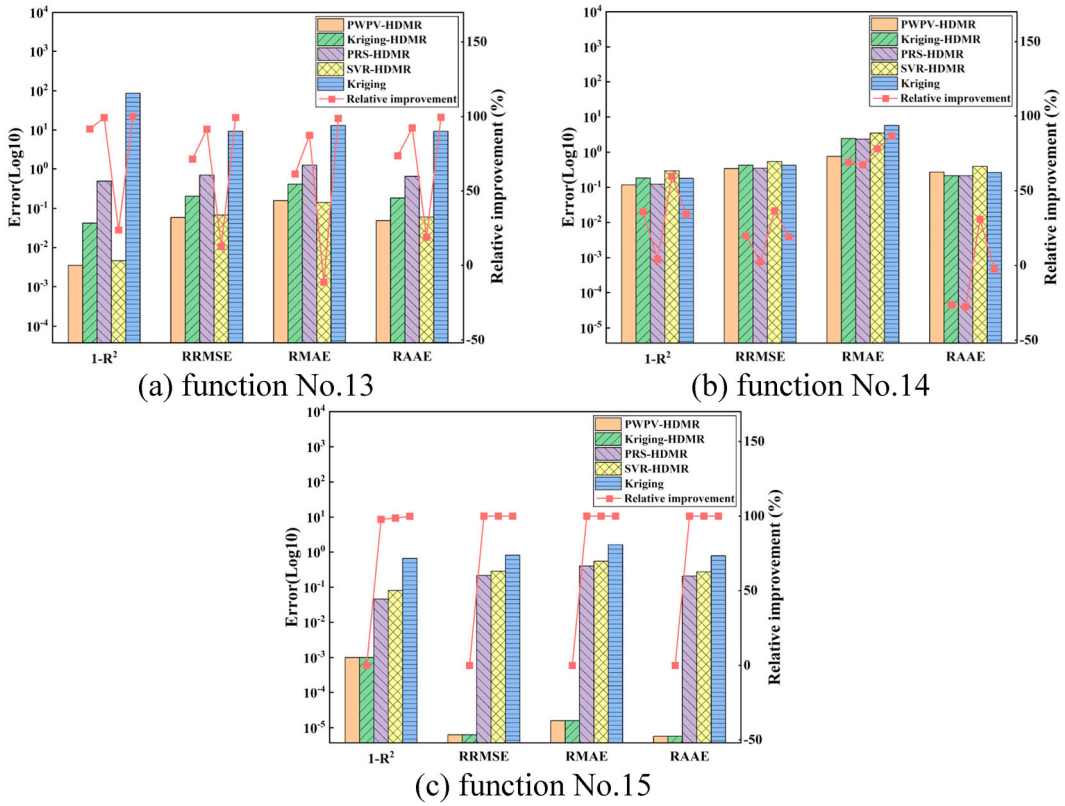


Figure 4. Modelling accuracy and relative improvement of the pointwise weighting prediction variance–high-dimensional model representation (PWPV-HDMR) (40 dimensions): (a) function no. 13; (b) function no. 14; (c) function no. 15. HDMR = high-dimensional model representation; PRS = polynomial response surface; SVR = support vector regression; R^2 = coefficient of determination; RRMSE = relative root mean square error; RMAE = relative maximum absolute error; RAAE = relative average absolute error.

Table 1. Comparative results of the modelling accuracy (30 dimensions).

Function	Surrogates	R^2	RRMSE	RMAE	RAAE	NOP
10	PWPV-HDMR	9.96E-01	6.12E-02	1.67E-01	4.88E-02	181 + 2
	Kriging-HDMR	9.56E-01	2.09E-01	5.00E-01	1.83E-01	
	PRS-HDMR	6.16E-01	6.18E-01	1.33E+00	5.65E-01	
	SVR-HDMR	9.95E-01	6.92E-02	1.64E-01	5.99E-02	
	Kriging	<i>-6.34E+01</i>	<i>8.02E+00</i>	<i>1.14E+01</i>	<i>7.96E+00</i>	
11	PWPV-HDMR	9.56E-01	2.10E-01	1.43E+00	1.55E-01	181 + 3917
	Kriging-HDMR	9.10E-01	3.01E-01	<i>3.23E+00</i>	1.38E-01	
	PRS-HDMR	9.37E-01	2.51E-01	1.21E+00	1.95E-01	
	SVR-HDMR	<i>7.59E-01</i>	<i>4.90E-01</i>	2.77E+00	<i>3.57E-01</i>	
	Kriging	8.97E-01	3.21E-01	3.05E+00	2.28E-01	
12	PWPV-HDMR	10.00E-01	5.00E-05	1.36E-04	4.40E-05	4098 121 + 2
	Kriging-HDMR	10.00E-01	5.00E-05	1.36E-04	4.40E-05	
	PRS-HDMR	9.99E-01	2.73E-02	1.15E-01	2.18E-02	
	SVR-HDMR	9.36E-01	2.53E-01	4.92E-01	2.38E-01	
	Kriging	<i>8.14E-01</i>	<i>4.31E-01</i>	<i>8.49E-01</i>	<i>4.06E-01</i>	

Note: Best results are shown in bold; worst results in italic.

PWPV-HDMR = pointwise weighting prediction variance–high-dimensional model representation; HDMR = high-dimensional model representation; PRS = polynomial response surface; SVR = support vector regression; R^2 = coefficient of determination; RRMSE = relative root mean square error; RMAE = relative maximum absolute error; RAAE = relative average absolute error; NOP = number of sample points.

Table 2. Comparative results of the modelling accuracy (40 dimensions).

Function	Surrogates	R^2	RRMSE	RMAE	RAAE	NOP
13	PWPV-HDMR	9.97E-01	5.87E-02	1.58E-01	4.87E-02	321 + 2
	Kriging-HDMR	9.58E-01	2.04E-01	4.06E-01	1.83E-01	
	PRS-HDMR	5.14E-01	6.95E-01	1.25E+00	6.42E-01	
	SVR-HDMR	9.95E-01	6.72E-02	1.42E-01	6.01E-02	
	Kriging	<i>-8.57E+01</i>	<i>9.31E+00</i>	<i>1.30E+01</i>	<i>9.25E+00</i>	
14	PWPV-HDMR	8.82E-01	3.43E-01	7.62E-01	2.72E-01	281 + 3122
	Kriging-HDMR	8.16E-01	4.28E-01	2.46E+00	2.15E-01	
	PRS-HDMR	8.77E-01	3.51E-01	2.34E+00	2.13E-01	
	SVR-HDMR	<i>7.07E-01</i>	<i>5.41E-01</i>	3.49E+00	<i>3.94E-01</i>	
	Kriging	8.20E-01	4.24E-01	<i>5.77E+00</i>	2.65E-01	
15	PWPV-HDMR	10.00E-01	6.27E-06	1.59E-05	5.69E-06	161 + 2
	Kriging-HDMR	10.00E-01	6.27E-06	1.59E-05	5.69E-06	
	PRS-HDMR	9.54E-01	2.15E-01	3.99E-01	2.07E-01	
	SVR-HDMR	9.19E-01	2.84E-01	5.45E-01	2.72E-01	
	Kriging	<i>3.38E-01</i>	<i>8.13E-01</i>	<i>1.63E+00</i>	<i>7.80E-01</i>	

Note: Best results are shown in bold; worst results in italic.

PWPV-HDMR = pointwise weighting prediction variance–high-dimensional model representation; HDMR = high-dimensional model representation; PRS = polynomial response surface; SVR = support vector regression; R^2 = coefficient of determination; RRMSE = relative root mean square error; RMAE = relative maximum absolute error; RAAE = relative average absolute error; NOP = number of sample points.

From the histogram and line chart in Figure 4, it can be observed that the PWPV-HDMR model performs the best in case 13, shows similar performance to the kriging-HDMR model in case 15 and maintains the optimal overall ranking in case 14.

In general, in each case, there is at least one well-performing basic HDMR model, and the improvement of PWPV-HDMR relative to these models is much smaller than that of other models. It is noteworthy that these models vary for each case, demonstrating the ability of the PWPV-HDMR model to learn and surpass promising basic HDMR models when facing different problems. The results and analysis for the 10-dimensional and 20-dimensional cases are provided in Appendix B, leading to similar conclusions.

3.2. Significance analysis

In this subsection, significance analysis of the results will be conducted from two aspects: average ranking differences and impact of dimensions. Table 3 presents the average ranking of model predictive performance for different test cases. It can be seen that the overall average ranking of the PWPV-HDMR model is the highest, while the average rankings of kriging-HDMR, PRS-HDMR, SVR-HDMR and the kriging model decrease successively.

In this article, the post-hoc Nemenyi testing method (significance level $\alpha = 0.05$) is used to analyse the significance of average ranking differences among the five surrogate models on the numerical test cases, as shown in Table 4. Figure 5 presents the corresponding heatmap for significance analysis. In the figure, the greater the number of ‘*’ symbols, the more significant the difference between the two surrogate models. It can be observed that PWPV-HDMR exhibits significant differences in predictive performance compared to the other four surrogate models, with particularly pronounced distinctions from PRS-HDMR, SVR-HDMR and kriging models. Furthermore, the significance of differences among the three basic HDMR models is not substantial. Except for the SVR-HDMR model, there is a significant difference in the performance between the kriging model and the other basic HDMR models.

From Tables A1–A4 (Appendix A), it is evident that cases 1, 6, 10 and 13, and cases 3, 8, 11 and 14, differ only in dimensions. As illustrated in Figure 6, to further investigate the influence of dimensions on model accuracy, a line chart depicting the improvement in accuracy of the PWPV-HDMR model as dimensions vary, relative to the other four models, is presented. The graphs illustrate that the

Table 3. Average ranking of models for different test cases.

Function	PWPV-HDMR	Kriging-HDMR	PRS-HDMR	SVR-HDMR	Kriging
1 (10D)	1.75	3	4	1.25	5
2 (10D)	1.5	2.75	3.25	4.25	3.25
3 (10D)	1.25	4	2.25	2.5	5
4 (10D)	1.25	3	2	4.5	4.25
5 (10D)	1.125	1.875	3	4	5
6 (20D)	1.25	3	4	1.75	5
7 (20D)	1	2	3	4	5
8 (20D)	1	3	2.25	5	3.5
9 (20D)	2	3	1	4	5
10 (30D)	1.25	3	4	1.75	5
11 (30D)	1.5	3	2	4.5	4
12 (30D)	1.5	1.5	3	4	5
13 (40D)	1.25	3	4	1.75	5
14 (40D)	1.75	3.25	1.75	4.75	3.5
15 (40D)	1.5	1.5	3	4	5
Average	1.3917	2.7250	2.8333	3.4667	4.5667

Note: PWPV-HDMR = pointwise weighting prediction variance–high-dimensional model representation; HDMR = high-dimensional model representation; PRS = polynomial response surface; SVR = support vector regression.

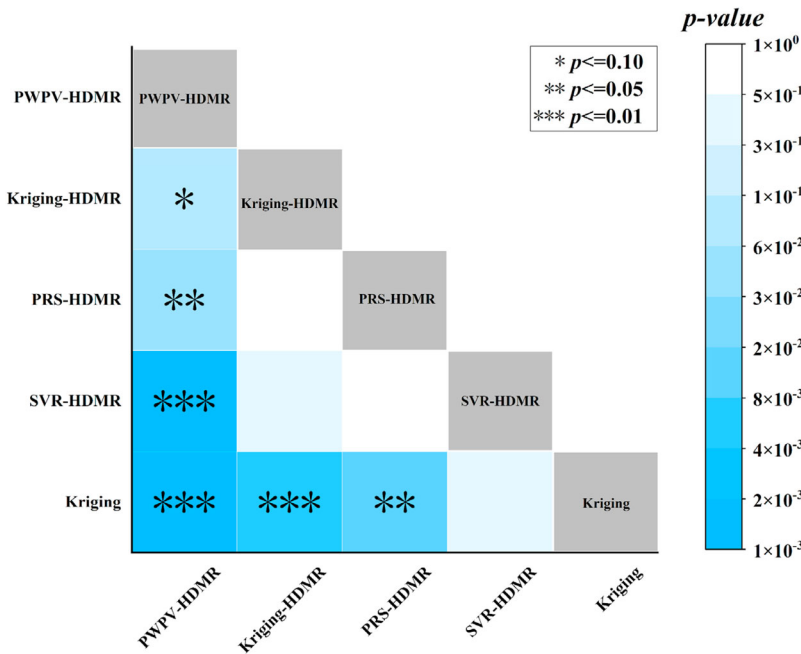


Figure 5. Heatmap of the significance of differences among the five surrogate models. PWPV-HDMR = pointwise weighting prediction variance–high-dimensional model representation; HDMR = high-dimensional model representation; PRS = polynomial response surface; SVR = support vector regression.

relative improvements of the PWPV-HDMR model remain relatively constant with increasing dimensions. Furthermore, through a one-way analysis of variance (ANOVA) (significance level $\alpha = 0.05$), $p_1 = 0.999$ and $p_2 = 0.846$ were obtained. Therefore, it can be concluded that the degree of improvement of the PWPV-HDMR model relative to the other four models is not significantly related to the dimensionality.

Table 4. p -Values for the significance test of the differences among the five surrogate models.

i	Hypothesis	p_i -Value
1	PWPV-HDMR vs Kriging-HDMR	8.21E-02
2	PWPV-HDMR vs PRS-HDMR	3.77E-02
3	PWPV-HDMR vs SVR-HDMR	1.00E-03
4	PWPV-HDMR vs Kriging	1.00E-03
5	Kriging-HDMR vs PRS-HDMR	9.00E-01
6	Kriging-HDMR vs SVR-HDMR	4.16E-01
7	Kriging-HDMR vs Kriging	5.93E-03
8	PRS-HDMR vs SVR-HDMR	5.86E-01
9	PRS-HDMR vs Kriging	1.57E-02
10	SVR-HDMR vs Kriging	4.52E-01

Note: PWPV-HDMR = pointwise weighting prediction variance–high-dimensional model representation; HDMR = high-dimensional model representation; PRS = polynomial response surface; SVR = support vector regression.

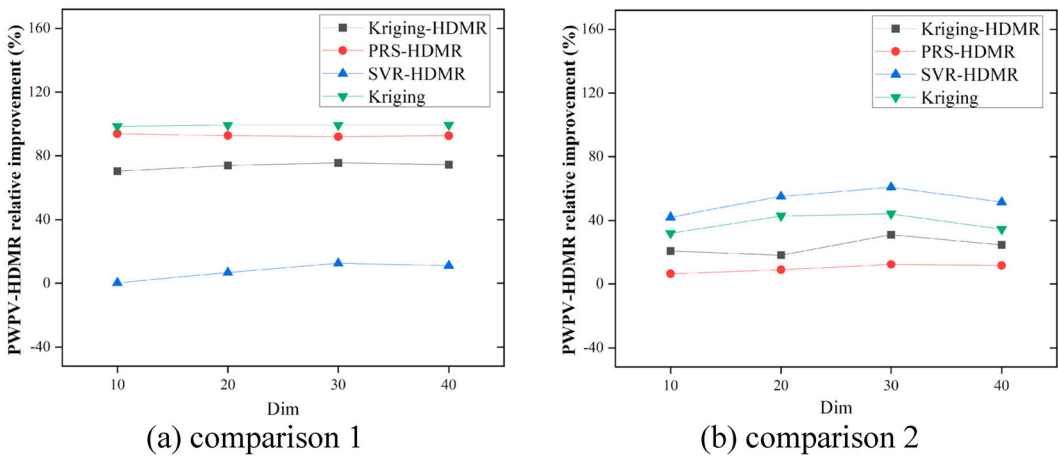


Figure 6. Relative improvement of the pointwise weighting prediction variance–high-dimensional model representation (PWPV-HDMR) with changing dimensions: (a) comparison 1; (b) comparison 2. HDMR = high-dimensional model representation; PRS = polynomial response surface; SVR = support vector regression; Dim = dimensions.

4. CAD/CFD process for hydrostatic resistance optimization of KCS models

4.1. Basic information on the mother ship

The KCS, characterized by a bulbous bow, is a standard modern 3600 TEU (twenty-foot equivalent unit) container ship. It exhibits distinct flow-field characteristics at the stern, making it suitable for flow-field analysis and the validation of CFD technology. Various data and experimental results for the KCS can be obtained from Denmark's FORCE Technology company. The main parameters of the KCS are presented in Table 5, and the complete geometric model is shown in Figure 7(a). In this article, the primary focus of the research is on the resistance of the KCS in a towed state in calm water, with a design speed of 24 knots corresponding to a Froude number of 0.26. In this scenario, the ship's propeller structure does not provide propulsion and is omitted. In addition, to facilitate the geometric deformation reconstruction and parameterized design of the hull, simplifications have been made in the area around the propeller shaft. The scaled-down model after these simplifications is depicted in Figure 7(b).

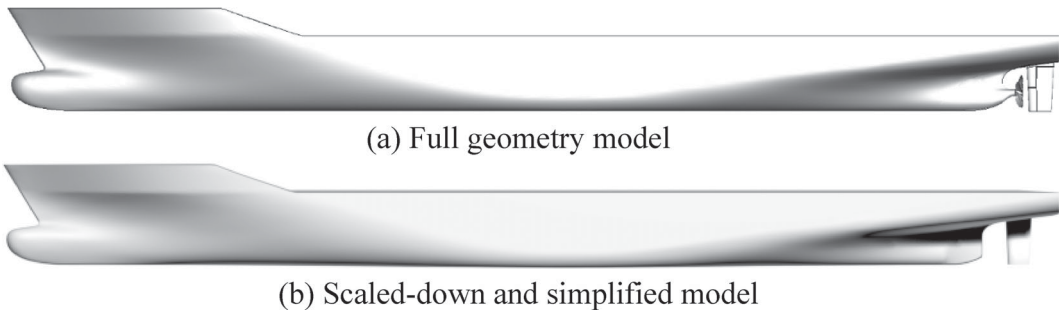


Figure 7. Geometric model of the KRISO Container Ship (KCS): (a) full geometric model; (b) scaled-down and simplified model.

Table 5. Main particulars of the KRISO Container Ship (KCS).

Scale	1.000	1/31.599
Length between perpendiculars (L_{BP})	230.0 m	7.2786 m
Maximum beam of waterline (B_{WL})	32.2 m	1.0190 m
Depth (D)	19.0 m	0.6013 m
Draft (T)	10.8 m	0.3418 m
Displacement volume (∇)	52,030 m ³	1.6490 m ³
Wetted surface area without rudder (S)	9539 m ²	9.55275 m ²
Longitudinal centre of buoyancy (LCB) (% L_{BP})	48.52	48.52
Longitudinal centre of gravity (L_{CG}) (from stern)	111.6 m	3.532 m
Moment of inertia (K_{xx}/B)	0.40	0.40
Moment of inertia ($K_{yy}/L_{BP}, K_{zz}/L_{BP}$)	0.25	0.25
Design speed (U)	24.0 knots	2.196 m/s
Fn (based on L_{BP})	0.26	0.26

4.2. Parameterized design of the KCS using the FFD method

The FFD technique (Sederberg and Parry 1986) is a highly flexible geometric reconstruction method that allows for the free deformation of entities of arbitrary geometric shapes. To discretize the hull surface into the FFD control body, the KCS geometric file is converted into the STereoLithography (STL) format, representing the hull surface as a discrete set of triangular facets, as shown in Figure 8. Considering the influence of various sections of the hull shape on wave resistance, frictional resistance and viscous pressure resistance for medium- to high-speed vessels, a parameterization of the FFD was carried out to discretize the design space. This includes deformations in five different directions: hull length (Veritas 2009), design waterline width (Meng *et al.* 2010) and bilge width (Thiagarajan and Braddock 2010) in three global directions, as well as the bulbous bow (Mahmood and Huang 2012) and stern (Park and Chun 2009) in two local directions. Collectively, these are referred to as design parameters. Each design parameter consists of six parameter variables, named controlled parameters. Consequently, the hull shape reconstruction involves a total of 30 design variables, making it a high-dimensional problem with 30 dimensions. Figure 9 illustrates the positions of the controlled parameters in the global direction.

In this article, the FFD reconstruction of the ship model is accomplished through a design program written in the C# language, and the specific operational process is illustrated in Figure 10. It should be emphasized that during the deformation process, adjustments are first made in two local directions, followed by deformations in three global directions. This sequence is designed to prevent significant relative displacement of the ship's region contained in the control body used for local deformation after global deformation. A comparison between the local and global control bodies is shown in Figure 11, with specific parameters detailed in Table 6.

To ensure that the ship model meets preliminary design and feasibility requirements after deformation, the range of values for the 30 design variables was determined using the displacement transfer



Figure 8. STereolithography file of the KRISO Container Ship (KCS) model.



Figure 9. Controlled parameter positions in the global directions.

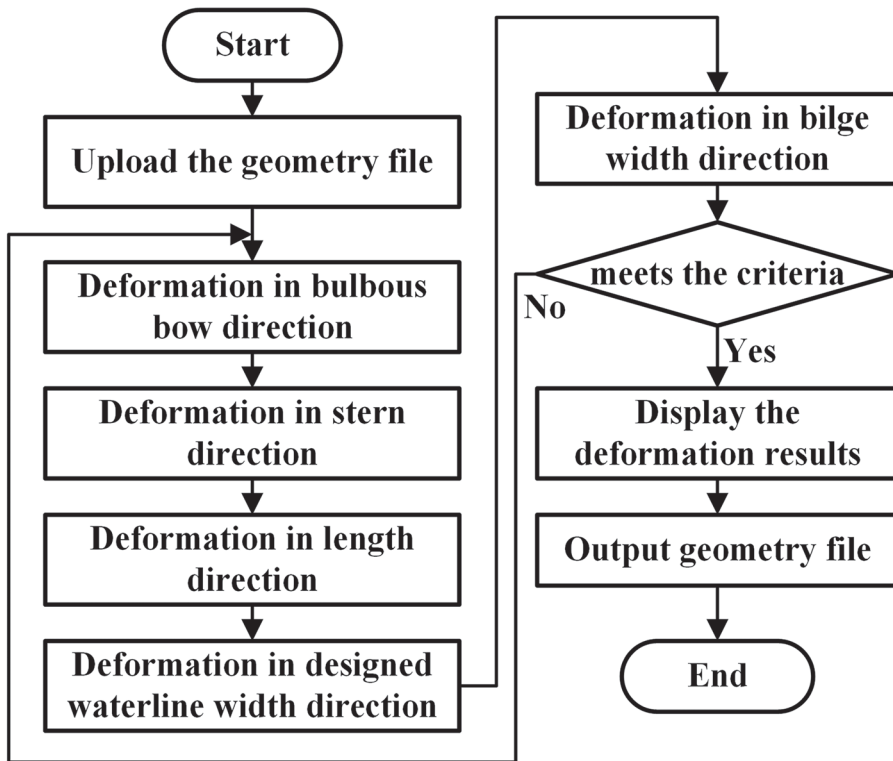


Figure 10. Flowchart of the free-form deformation (FFD) reconstruction of the ship model.

method, curve feature constraints and practical conditions, as presented in Table 7. In this table, the controlled parameters for the design parameters in the global controlled area direction share the same names. The numerical values in the value range column of the table signify that when the controlled parameter is set to 0.01, it represents a deformation size of 1% of the total length of the hull.

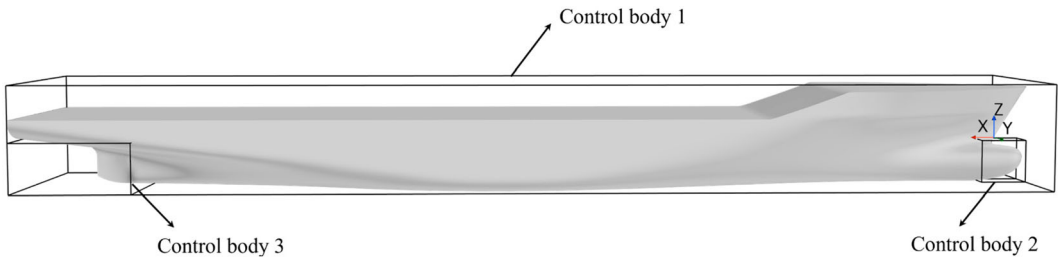


Figure 11. Comparison between the global and local control bodies (global: control body 1; local: control bodies 2 and 3).

Table 6. Parameters of control bodies.

Control body	Axial	Minimum	Maximum	No. of control points	Control area
Control body 1	X	−0.2101 m	7.0685 m	7	Global
	Y	−0.4822 m	0.4822 m	7	
	Z	−0.3238 m	0.4317 m	15	
Control body 2	X	−0.2095 m	0.1171 m	7	Bulbous bow
	Y	−0.0708 m	0.0708 m	7	
	Z	−0.3238 m	−0.0138 m	7	
Control body 3	X	6.2292 m	7.0685 m	7	Stern part
	Y	−0.4822 m	0.4822 m	7	
	Z	−0.3238 m	0.0344 m	7	

Table 7. Range of values for controlled parameters.

Control body	Controlled area	Design parameters	Controlled parameters	Value range
Control body 1	Global	Hull length	Bow part	[−0.005,0.002]
			Entrance part	[−0.01,0.01]
			Forward shoulder part	[−0.01,0.01]
			After shoulder part	[−0.01,0.01]
			Run part	[−0.01,0.01]
			Stern part	[−0.005,0.005]
		Designed waterline width	Bow part	[−0.01,0.01]
			Entrance part	[−0.01,0.01]
			Forward shoulder part	[−0.01,0.01]
			After shoulder part	[−0.01,0.01]
			Run part	[−0.01,0.01]
			Stern part	[−0.01,0.01]
		Bilge width	Bow part	[−0.01,0.01]
			Entrance part	[−0.01,0.01]
			Forward shoulder part	[−0.01,0.01]
After shoulder part	[−0.01,0.01]			
Run part	[−0.01,0.01]			
Stern part	[−0.01,0.01]			
Control body 2	Local	Bulbous bow	Foremost Δx	[−0.005,0.003]
			Foremost Δy	[−0.01,0.01]
			Foremost Δz	[−0.004,0.003]
			Width Δy	[−0.005,0.005]
			Bottom Δy	[−0.005,0.01]
			Bottom Δz	[−0.005,0.005]
Control body 3	Local	Stern part	Stern closure plate Δx	[−0.01,0.01]
			Front lower end Δy	[−0.01,0.01]
			Front lower end Δz	[−0.006,0.006]
			Front upper end Δy	[−0.01,0.01]
			Rear upper end Δy	[−0.01,0.01]
			Rear upper end Δz	[−0.006,0.006]

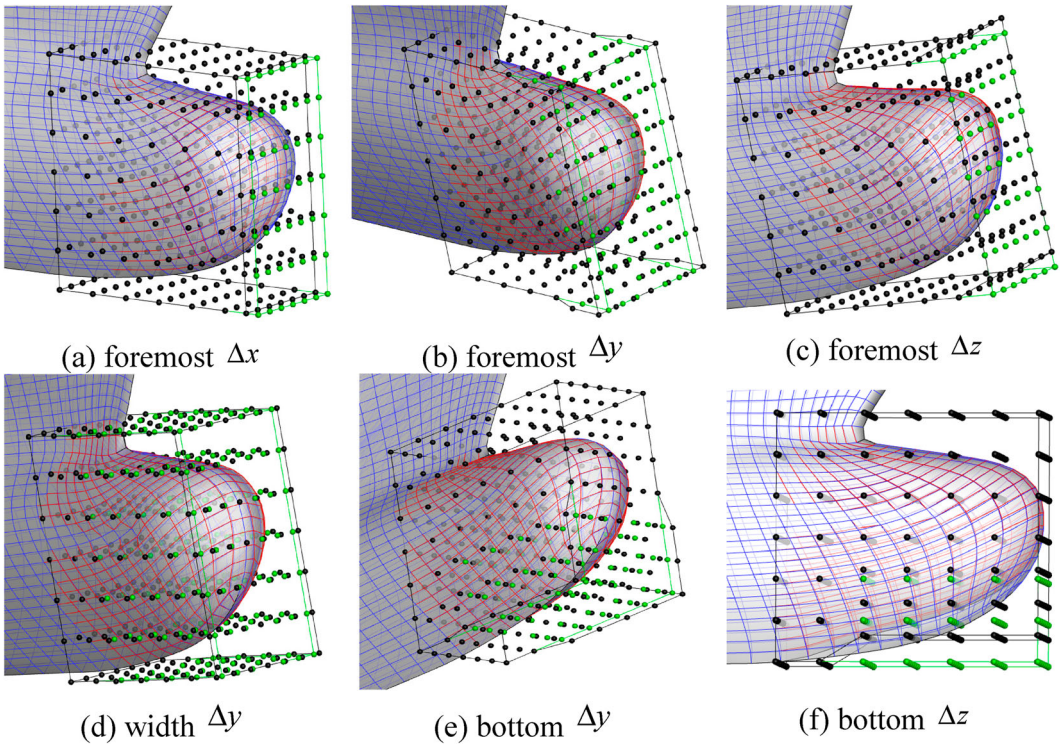


Figure 12. Comparison of the bulbous bow before and after deformation: (a) foremost Δx ; (b) foremost Δy ; (c) foremost Δz ; (d) width Δy ; (e) bottom Δy ; (f) bottom Δz .

Table 8. Example values for controlled parameters of the bulbous bow.

	Foremost Δx	Foremost Δy	Foremost Δz	Width Δy	Bottom Δy	Bottom Δz
Bulbous bow	0.001	0.001	0.001	0.001	0.001	0.001

Using the bulbous bow as an example of deformation, the values of its controlled parameters are adjusted as shown in Table 8. The comparison of the bulbous bow before and after deformation is illustrated in Figure 12, where the black points represent the control points after deformation and the light-colored surfaces depict the model after deformation. The deformation control process for the remaining four sections of design parameters is similar to that of the bulbous bow. Therefore, this article will achieve the parameterized design of the KCS by adjusting the values of the 30 controlled parameters from Table 7.

4.3. Static water resistance simulation of KCS models

In this article, the fluid dynamics simulation software STAR CCM+ is used to simulate the resistance of the KCS model in calm water under towing conditions.

4.3.1. Computational domain and boundary conditions

Owing to the geometric symmetry of the ship model, only half of the hull and the flow domain is used in the computational domain. Following the recommendations of International Towing Tank Conference (ITTC, 2011), the inlet boundary is located $2.25L_{BP}$ away from the stern, while the outlet boundary is located $3L_{BP}$ downstream to mitigate wave reflection from the boundaries. Taking cost

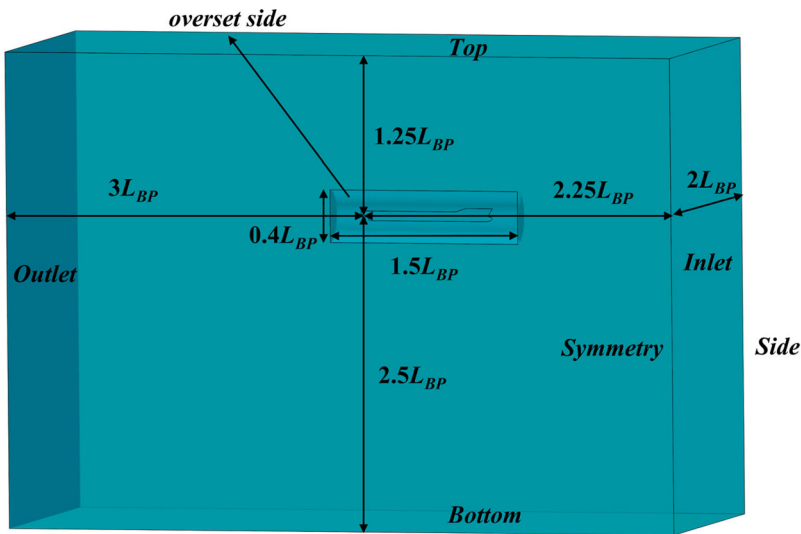


Figure 13. Computational domain and boundary conditions.

Table 9. Summary of boundary conditions.

Boundary name	Boundary condition
Inlet, top, bottom	Velocity inlet
Hull	No-slip wall condition
Symmetry, side	Symmetry plane
Overset-side	Overset mesh
Outlet	Pressure outlet

considerations into account, the ultimately determined computational domain is depicted in Figure 13. The summary of the boundary conditions is presented in Table 9.

4.3.2. Mesh generation

The volume mesh uses a trimmed cell remesher to facilitate refinement in areas such as the free water surface, wave systems and the ship hull by adjusting the control volumes with different mesh sizes. The boundary layer is set to six layers, with a total thickness of 0.02 m. In addition, overset mesh technology is used to accurately simulate the motion and attitude of the ship model. The generated global mesh is illustrated in Figure 14, and the locally refined mesh around the hull is shown in Figure 15.

4.3.3. Numerical methods

Considering that there are no frequent turbulent eddies or pulsations during static water towing of the ship, the Reynolds-averaged Navier–Stokes (RANS) equations are used to simulate turbulent flow in the flow field, with the application of the Menter’s shear stress transport $k-\omega$ turbulence model. Considering time accuracy, the pressure-implicit with splitting of operators (PISO) algorithm is used to solve the coupled equations of velocity and pressure. The dynamic fluid body interaction (DFBI) method is used for the 2-degree-of-freedom (DoF), *i.e.* sinkage and trim, prediction of the ship, while the volume of fluid (VOF) wave method is used for capturing the free liquid surface. Damping wave reflections are implemented to prevent wave reflections from the boundary and abrupt grid transitions.

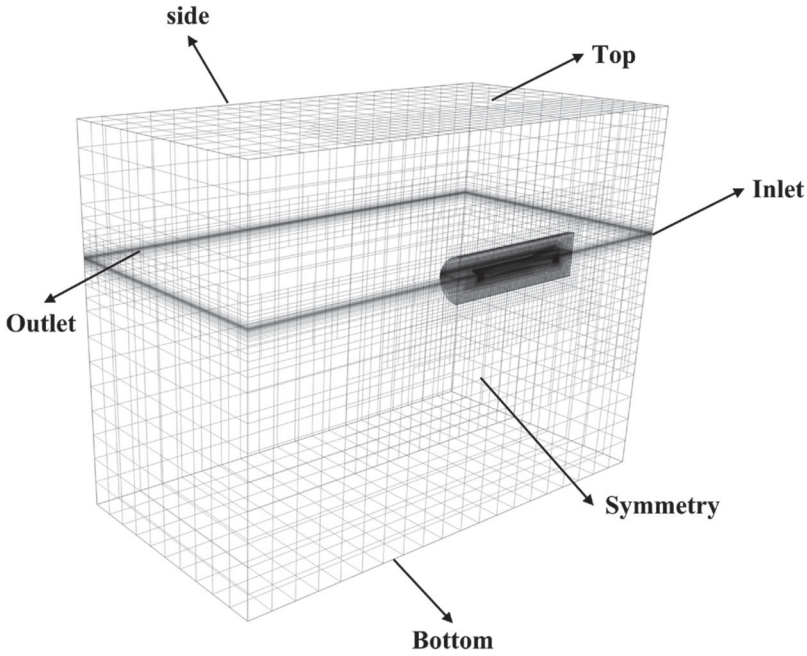


Figure 14. Global mesh.

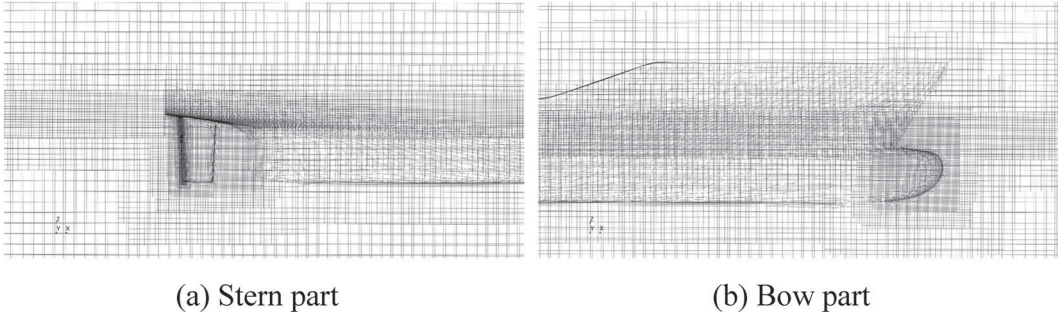


Figure 15. Locally refined mesh around the hull: (a) stern part; (b) bow part.

4.3.4. Independence verification

In this study, the non-dimensional total resistance coefficient C_T will be used to analyse the accuracy of the total resistance of the ship. C_T is calculated using the following formula:

$$C_T = \frac{F_X}{\frac{1}{2}\rho U^2 S} \quad (15)$$

where F_X is the total resistance measured in the X -direction in the Earth coordinate system. The density of water (ρ) is 999.5 kg/m^3 , and the values of the remaining parameters in Equation (15) are shown in Table 5. The simulated resistance iteration curve is shown in Figure 16. After sufficient convergence has been achieved in the calculations, the last 10 samples of the time history are used to calculate the average total resistance.

4.3.4.1. Time independence verification. Following the recommendations of ITTC (2011a), for the calculation of resistance in calm water, the suggested time step is $\Delta t = 0.005 \sim 0.01 \frac{L_{BP}}{U}$. Rounding

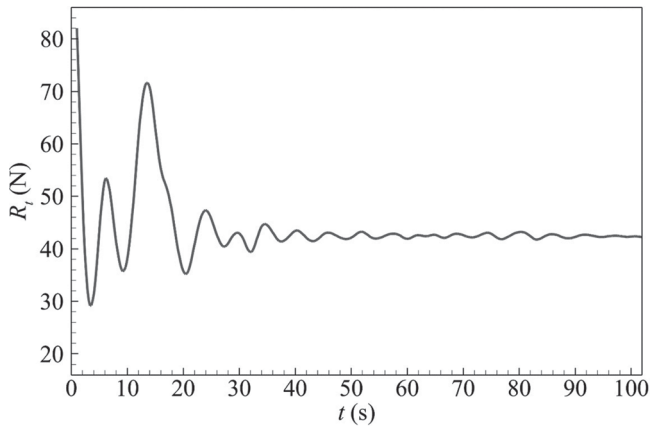


Figure 16. Simulated resistance iteration curve.

Table 10. Resistance results for different time steps.

Δt (s)	C_T	Error (% of Experiment)
0.04	0.003647	-1.72
0.03	0.003682	-0.80
0.02	0.003704	-0.19
Experiment	0.003711	-

Table 11. Results for different grid schemes.

Scheme	Total grid number (w)	C_T	Error (% of Experiment)
Coarse	59.7	0.003762	1.37
Medium	82.4	0.003682	-0.80
Fine	144.2	0.003689	-0.59
Experiment	-	0.003711	-

up, $\Delta t = 0.02\text{--}0.04$ s was obtained. Table 10 presents the resistance results for different time steps with a mesh count of 824,000, along with the towing tank experiment results in calm water for the model conducted by Simonsen *et al.* (2013).

It can be observed that further reducing the time step beyond 0.03 s does not yield significant improvements in accuracy. Considering the trade-off between accuracy and computational cost, a time step of 0.03 s is chosen for the subsequent simulations.

4.3.4.2. Grid independence verification. In Table 11, the calculated results for three grid schemes with $\Delta t = 0.03$ s are listed to verify grid independence.

Compared with the experimental results, the errors in the results of both the medium and fine grid schemes are each less than 1%, which is within an acceptable range for engineering applications. Considering that the medium grid scheme is more efficient, the grid division in the subsequent studies will be based on the settings of the medium grid. This also means that in the subsequent optimization problem, the initial value of the resistance coefficient is chosen as 0.003682, and the initial value of the resistance is selected as 41.874 N.

5. Optimization and analysis of KCS model

5.1. Optimization objective and constraints

The optimization objective of this study is to minimize the static water towing resistance of KCS. The design variables X consist of 30 controlled parameters, and their ranges are specified in Table 7. The design displacement, wetted surface area without rudder and longitudinal centre of buoyancy of the ship are used as constraints, stipulating that their relative changes in the optimized ship do not exceed 1% compared to the original ship. In summary, the mathematical expression of the ship's low-resistance optimization problem is as shown in Equation (16):

$$\begin{aligned} & \text{find } X(x_1, \dots, x_{30}) \\ & \text{min } R_T(X) \text{ at } Fr = 0.26 \\ & \text{s.t. } \frac{|\Delta - \Delta^{opt}(X)|}{\Delta} \leq 1\%, \frac{|S - S^{opt}(X)|}{S} \leq 1\%, \frac{|L_{CB} - L_{CB}^{opt}(X)|}{L_{CB}} \leq 1\% \end{aligned} \quad (16)$$

where the resistance R_T is predicted using the surrogate model; Δ , S and L_{CB} represent the design displacement, wetted surface area without rudder and longitudinal centre of buoyancy of the original ship, calculated as 1.6492 m³, 9.52259 m² and 48.46(% L_{BP}), respectively, using STAR-CAD software; and $\Delta^{opt}(X)$, $S^{opt}(X)$ and $L_{CB}^{opt}(X)$ represent the corresponding values of the optimized ship.

5.2. Ship resistance sampling and construction of surrogate models

The entire process of FFD, simulation and sequential modelling was implemented through C#, Java and Python programs developed in this study, as illustrated in Figure 17. The simulations in this article were performed using an Intel[®] Core[™] i9-9820X CPU @ 3.30 GHz processor for 10-core parallel computing. Owing to varying convergence times for each simulation, the runtime is determined by the number of iterations. Specifically, the average runtime for 20,000 iterations is around 2.7 h. Therefore, considering both the collection time of sample points and the accuracy of the model, when the relative error between the predicted value and the true value of new sample points is less than 2% (usually taken as 1%), it is considered that the ensemble surrogate model has converged. According to this setting, 303 sample points were collected during the construction of the first-order HDMR model, and 184 sample points were collected during the construction of the second-order HDMR model. Fifty validation points were collected at once through optimized Latin hypercube sampling. Thus, the total simulation time is approximately $537 * 2.7 \text{ h} = 1449.9 \text{ h}$.

To assess the predictive performance of the PWPV-HDMR, kriging-HDMR, PRS-HDMR, SVR-HDMR and kriging models, all constructed with the same sample points, the results are shown in Figure 18 and Table 12. It can be observed that the HDMR models, especially the PWPV-HDMR model, outperformed the kriging model globally and locally. The kriging-HDMR achieved the second-best performance among most indicators, excluding the local prediction metric RMAE. Therefore, in the next section, the optimization algorithm will be applied to the PWPV-HDMR model, with the second-best kriging-HDMR model used for comparison.

5.3. Analysis of design optimization results

The DE algorithm is a highly useful global optimization algorithm that seeks the global optimum through the competition and cooperation among individuals. Previous studies (Gong, Cai, and Liang 2014; Mallipeddi *et al.* 2011; Qin, Huang, and Suganthan 2008) show that the DE algorithm performs well in handling high-dimensional optimization problems, and some research (Brizzolara, Bruzzone, and Tincani 2005; L. Wang *et al.* 2015) has also applied it to the design of ship forms. The DE algorithm is used to seek the optimal solution, and its basic parameter settings are shown in Table 13.

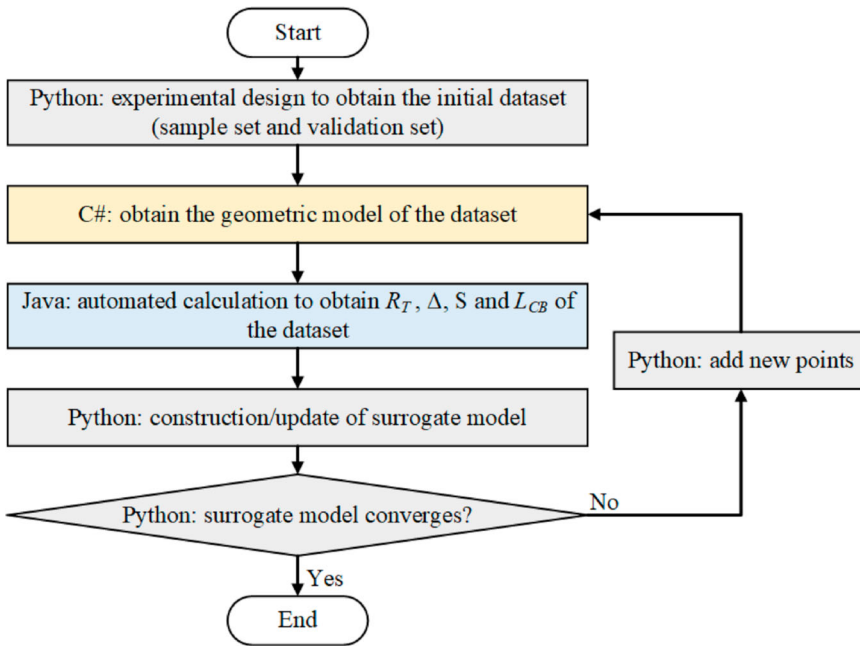


Figure 17. Flowchart of the construction of the resistance prediction surrogate model for the KRISO Container Ship (KCS) model.

Table 12. Performance of the five models for resistance prediction.

Surrogates	R^2	RRMSE	RMAE	RAAE
PWPV-HDMR	8.24E-01	5.35E-01	1.09E+00	3.35E-01
Kriging-HDMR	6.96E-01	5.36E-01	1.43E+00	3.87E-01
PRS-HDMR	4.69E-01	7.29E-01	1.48E+00	4.27E-01
SVR-HDMR	6.16E-01	6.89E-01	1.26E+00	4.01E-01
Kriging	<i>-2.14E+00</i>	<i>1.52E+00</i>	<i>1.70E+00</i>	<i>1.13E+00</i>

Note: Best results are shown in bold; worst results in italic.

PWPV-HDMR = pointwise weighting prediction variance–high-dimensional model representation; HDMR = high-dimensional model representation; PRS = polynomial response surface; SVR = support vector regression; R^2 = coefficient of determination; RRMSE = relative root mean square error; RMAE = relative maximum absolute error; RAAE = relative average absolute error; NOP = number of sample points.

Table 13. Optimization parameters of the KRISO Container Ship (KCS).

Parameter	Value
Population	300
Maximum iteration	1000
Crossover rate	0.3
Mutation rate	0.8

To ensure the robustness of the optimization results, the optimization process based on the PWPV-HDMR and kriging-HDMR models was repeated 100 times, with the minimum resistance result selected from each set as the final optimization result. The optimization results based on PWPV-HDMR are referred to as ‘Opt-PH’ and those based on kriging-HDMR are referred to as ‘Opt-KH’, with specific controlled parameter values shown in Tables 14 and 15. The resistance prediction results for ‘Opt-PH’ and ‘Opt-KH’ are 39.8553 (1.5751×10^{-3}) and 39.7863 (3.8306×10^{-3}) respectively,

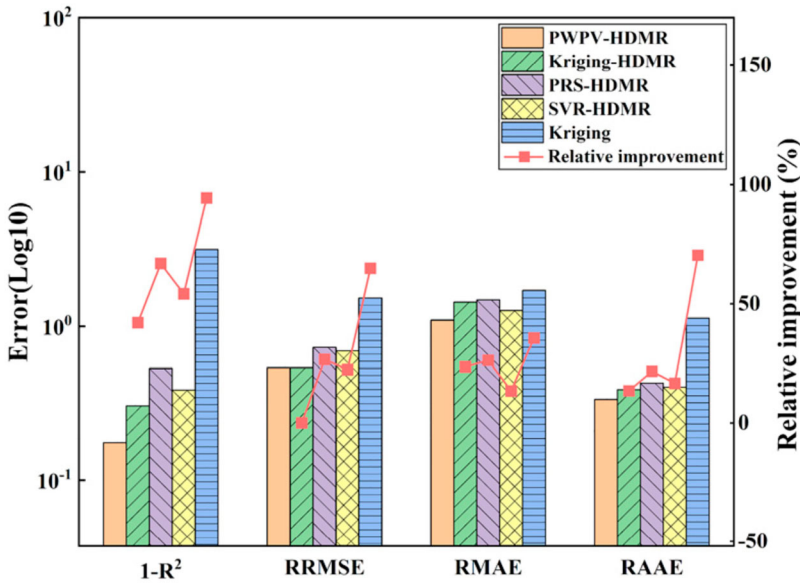


Figure 18. Performance of the five models for resistance prediction. PWPV-HDMR = pointwise weighting prediction variance–high-dimensional model representation; HDMR = high-dimensional model representation; PRS = polynomial response surface; SVR = support vector regression; R^2 = coefficient of determination; RRMSE = relative root mean square error; RMAE = relative maximum absolute error; RAAE = relative average absolute error.

Table 14. Optimization results using the pointwise weighting prediction variance–high-dimensional model representation (PWPV-HDMR) model (Opt-PH).

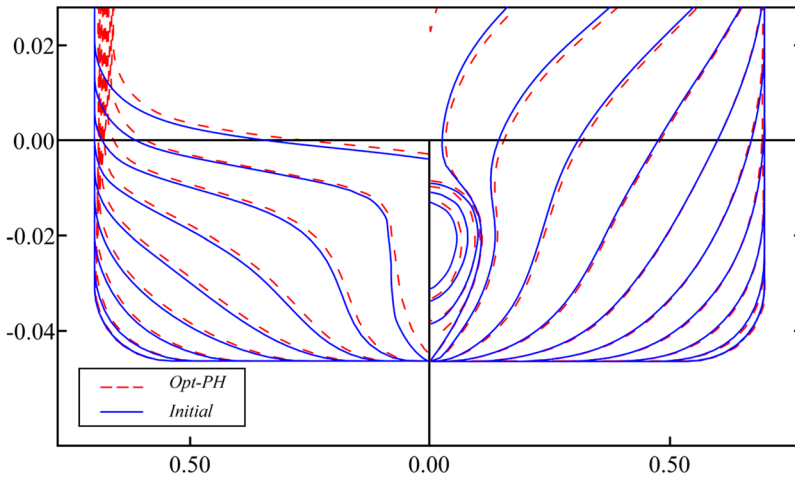
Design parameter	Controlled parameter 1	Controlled parameter 2	Controlled parameter 3	Controlled parameter 4	Controlled parameter 5	Controlled parameter 6
Hull length	−0.0041	−0.0075	0.01	−0.0013	−0.0087	0.0013
Designed waterline width	0.002	0.0006	−0.0013	−0.0023	−0.008	−0.0075
Bilge width	−0.0013	0.0044	0.0025	0.0022	−0.0057	−0.01
Bulbous bow	−0.0025	−0.0088	−0.0014	0.0027	0.0081	−0.0006
Stern part	0.0025	−0.0075	0.0057	0.0063	−0.0025	0.0029

Table 15. Optimization results using the kriging–high-dimensional model representation (HDMR) model (Opt-KH).

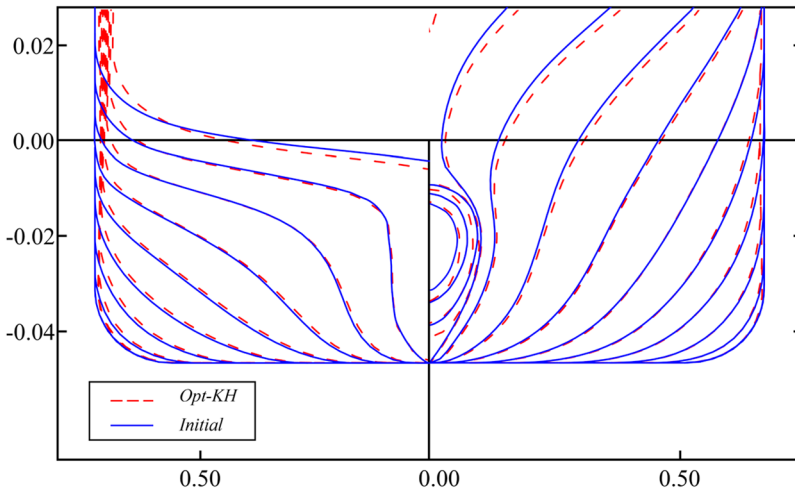
Design parameter	Controlled parameter 1	Controlled parameter 2	Controlled parameter 3	Controlled parameter 4	Controlled parameter 5	Controlled parameter 6
Hull length	−0.0043	−0.0075	0.01	−0.0013	0.0013	0.0015
Designed waterline width	0.0063	0.0013	−0.0017	−0.0042	−0.0025	−0.0079
Bilge width	−0.0013	0.005	0.0025	0.0013	−0.0063	−0.01
Bulbous bow	−0.0025	−0.009	−0.0012	0.0013	0.0081	−0.0009
Stern part	0.0027	−0.0075	0.0015	0.0069	−0.0025	−0.0031

where the values in parentheses represent the standard deviation. It can be observed that the optimization results for both are relatively robust. The comparison of the transverse hull lines between the two optimized ship models and the mother ship model is shown in Figure 19.

Combining Figure 19 and Table 14, it can be observed that, in terms of local changes, the optimized ship model Opt-PH exhibits a noticeable forward movement and sharpening at the front end of the bulbous bow compared to the mother ship model. The rear end of the bulbous bow, on the other hand,



(a) Opt-PH



(b) Opt-KH

Figure 19. Comparison of the transverse hull lines between the mother ship and the optimized ship: (a) optimization results based on pointwise weighting prediction variance–high-dimensional model representation (Opt-PH); (b) optimization results based on kriging–high-dimensional model representation (Opt-KH).

widens. Towards the stern, there is a trend of expansion followed by contraction along the bow to stern direction. In terms of global changes, considering the prominent changes in length and designed waterline width, the front half of the hull shows a certain forward movement and widening at the bow and entrance part, while the forward shoulder part experiences some backward movement and narrowing. In the rear half of the hull, the after shoulder part and run part exhibit forward movement and contraction, while the stern experiences some backward movement and contraction. For the less pronounced bilge width direction of the hull, along the bow to stern, it primarily shows a trend of widening followed by narrowing.

Combining Figure 19 and Table 15, it can be seen that, in terms of local changes, the trends of Opt-KH are generally consistent with those of Opt-PH, but Opt-KH tends to be smaller in the bulbous

Table 16. Comparison of optimization results based on pointwise weighting prediction variance–high-dimensional model representation (Opt-PH) and kriging–high-dimensional model representation (Opt-KH).

	R_T^{Opt-PH}	R_T^{Opt-KH}	Δ_{Opt-PH}	Δ_{Opt-KH}	S^{Opt-PH}	S^{Opt-KH}	L_{CB}^{Opt-PH}	L_{CB}^{Opt-KH}
Prediction	39.8553	39.7863	–	–	–	–	–	–
Simulation	40.4293	40.8273	1.6509	1.6392	9.5940	9.4791	48.31	48.09
Error (%)	1.42	2.55	–	–	–	–	–	–
$\frac{R_T^0 - R_T}{R_T^0} \times 100\%$	3.5	2.5	–	–	–	–	–	–
$\frac{ \Delta - \Delta^{opt} }{\Delta} \times 100\%$	–	–	0.11	0.60	–	–	–	–
$\frac{ S - S^{opt} }{S} \times 100\%$	–	–	–	–	0.75	0.46	–	–
$\frac{ L_{CB} - L_{CB}^{opt} }{L_{CB}} \times 100\%$	–	–	–	–	–	–	0.30	0.76

Note: $R_T^0 = 41.874$ N

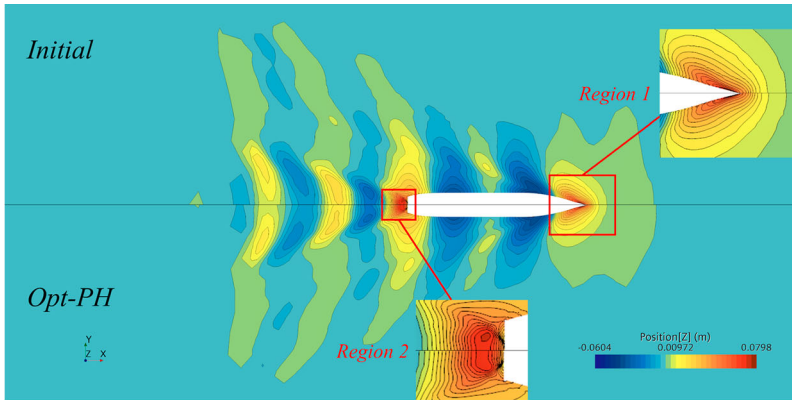
bow part and larger in the stern part compared to Opt-PH. In terms of global changes, except for the run part, there is little difference between the two in the length and bilge width directions, while in the designed waterline width direction, Opt-KH exhibits the same trend as Opt-PH but with more pronounced changes.

Using STAR-CCM+ to validate the optimized ship models mentioned above, the obtained results are shown in Table 16. First, it can be observed that the resistance value of both optimized ship models is lower than that of the mother ship. Furthermore, the design displacement, wetted surface area without rudder and longitudinal centre of buoyancy of the optimized ship models meet the constraint conditions. Secondly, although the resistance prediction result of Opt-KH is lower than that of Opt-PH, the actual simulation results are opposite: the optimization effect of the Opt-PH ship model is 3.5%, surpassing that of the Opt-KH ship model (2.5%), leading to a reduction in resistance of nearly 1.0%. Overall, it can be considered that both the PWPV-HDMR and kriging-HDMR models can be applied to the KCS resistance optimization problem, but the PWPV-HDMR model gives better prediction accuracy and optimization results.

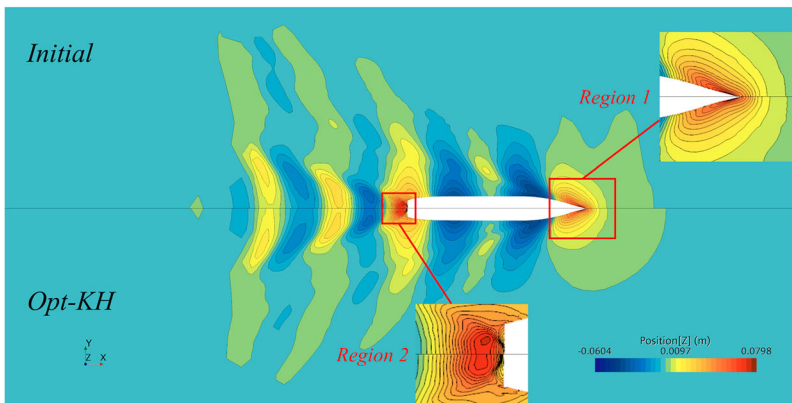
Figure 20 shows the free surface wave elevations of the two optimized ship models and the mother ship under the same operating conditions and physical time. In general, the bow wave system of the two optimized ship models, compared to the mother ship, exhibits a slight forward movement near the bow (region 1), but with little change in amplitude. Starting from the entrance part and extending to the region far from the stern, both the amplitude and area of the wave peaks and troughs have decreased. The difference between the two optimized ship models is that the forward movement of the bow wave system of the Opt-PH ship model is smaller, and, except in the area very close to the stern (region 2), the wave peak areas are smaller in other regions.

Figures 21–23 show the pressure distribution comparisons of the two optimized ship models and the mother ship for the entire ship, bow and stern, respectively. In general, the areas of high- and low-pressure regions for both optimized ship models are reduced compared to the mother ship in most regions. The Opt-PH ship model has the smallest areas of high- and low-pressure regions in the bow, entrance part, forward shoulder part and after shoulder part. However, the difference between Opt-PH and Opt-KH is not significant in the run part, and in the stern, the area is larger for Opt-PH than for Opt-KH.

Considering the results of the comprehensive analysis, it can be concluded that the pressure distribution and wave pattern of the Opt-PH ship model are generally better than those of the Opt-KH ship model and the parent ship, except for the stern part, where the pressure distribution is slightly inferior to that of the Opt-KH ship model. To further reduce ship resistance, it may be worthwhile to explore local optimization of the stern region in future work.



(a) The wave elevation comparison of the Opt-PH and Initial hulls.



(b) The wave elevation comparison of the Opt-KH and Initial hulls.

Figure 20. Comparison of the wave elevation of different hulls: (a) optimization results based on pointwise weighting prediction variance–high-dimensional model representation (Opt-PH) and initial hulls; (b) optimization results based on kriging–high-dimensional model representation (Opt-KH) and initial hulls.

6. Conclusions and future work

This article introduces a ship design optimization method especially for high-dimensional design variables. First, a pointwise weighted combination high-dimensional surrogate model based on prediction variance, called PWPV-HDMR, is proposed. This method is used to establish the relationship between ship hull parameters and hydrodynamic performance in ship design optimization. Subsequently, using PWPV-HDMR as the fitness function, the DE algorithm is introduced to identify promising ship hull parameters. The proposed method has been validated in determining the parameters of a low-resistance ship hull in static water towing for the KCS. The main conclusions of this study are as follows.

- (1) During the high-dimensional numerical study, the proposed PWPV-HDMR method exhibits good robustness and achieves comparable or superior approximation performance compared to the best basic HDMR models across different dimensionalities. This indicates that using PWPV-HDMR can reduce the risk of constructing inappropriate basis functions.
- (2) During the optimization and simulation validation process, the PWPV-HDMR model has a greater effect and higher accuracy than the kriging-HDMR model. This highlights the superiority of the PWPV-HDMR model in high-dimensional optimization problems compared to basic HDMR models and kriging models.

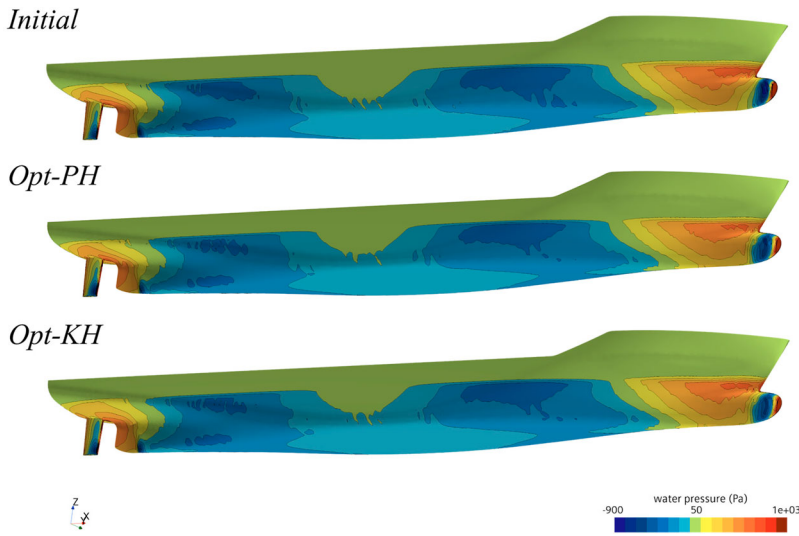


Figure 21. Pressure distribution for the entire ship. Opt-PH = optimization results based on pointwise weighting prediction variance–high-dimensional model representation model; Opt-KH = optimization results based on kriging–high-dimensional model representation.

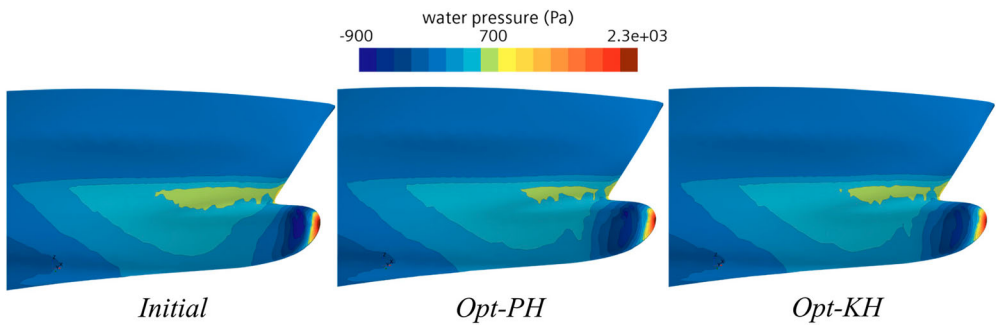


Figure 22. Pressure distribution for the bow. Opt-PH = optimization results based on pointwise weighting prediction variance–high-dimensional model representation model; Opt-KH = optimization results based on kriging–high-dimensional model representation.

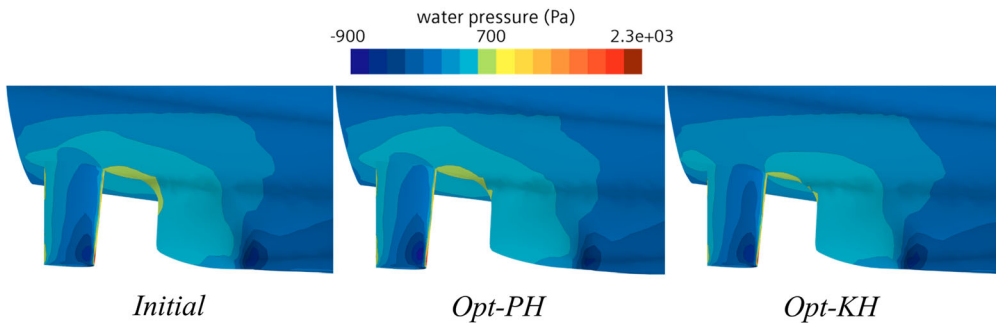


Figure 23. Pressure distribution for the stern. Opt-PH = optimization results based on pointwise weighting prediction variance–high-dimensional model representation model; Opt-KH = optimization results based on kriging–high-dimensional model representation.

During ship design optimization, a precise PWPV-HDMR model is first constructed, and then DE is used for optimization based on this model. However, this approach may lead to the arrangement of useless sampling points near the non-optimal point, which will affect the efficiency of optimization. For future research, it is crucial to explore optimization methods that dynamically update the surrogate model during the optimization process.

Disclosure statement

No potential conflict of interest was reported by the authors.

Data availability statement

The data that support the findings of this study are available from the corresponding author, J. X. Hu, upon reasonable request.

Funding

This research was supported by the National Key Research and Development Program of China [grant number 2023YFB3406900], the National Natural Science Foundation of China [grant numbers 52105254 and 52175231] and the Knowledge Innovation Program of Wuhan-Shuguang.

References

- Brizzolara, S., D. Bruzzone, and E. Tincani. 2005. "Automatic Optimization of a Trimaran Hull Form Configuration." In *8th International Conference on Fast Sea Transportation (FAST05)*, 136–145, Saint Petersburg, Russia.
- Chen, L., H. Wang, F. Ye, and W. Hu. 2019. "Comparative Study of HDMRS and Other Popular Metamodeling Techniques for High Dimensional Problems." *Structural and Multidisciplinary Optimization* 59 (1): 21–42. <https://doi.org/10.1007/s00158-018-2046-8>.
- Choo, C. T., J. H. Ang, S. Kuik, L. C. M. Hui, Y. Li, and C. Goh. 2020. "Ship Design with a Morphing Evolutionary Algorithm." In *2020 IEEE Congress on Evolutionary Computation (CEC)*, 1–8. IEEE.
- Diez, M., S. Volpi, A. Serani, F. Stern, and E. F. Campana. 2019. "Simulation-Based Design Optimization by Sequential Multi-criterion Adaptive Sampling and Dynamic Radial Basis Functions. Advances in Evolutionary and Deterministic Methods for Design, Optimization and Control in Engineering and Sciences." *Computational Methods in Applied Sciences* 48: 213–228.
- Evans, E., M. Scott, X. Li, and D. Thomas. 2015. "Hierarchical T-Splines: Analysis-Suitability, Bézier Extraction, and Application as an Adaptive Basis for Isogeometric Analysis." *Computer Methods in Applied Mechanics and Engineering* 284: 1–20. <https://doi.org/10.1016/j.cma.2014.05.019>.
- Feng, Y., Z. Chen, Y. Dai, F. Wang, J. Cai, and Z. Shen. 2018. "Multidisciplinary Optimization of an Offshore Aquaculture Vessel Hull Form Based on the Support Vector Regression Surrogate Model." *Ocean Engineering* 166:145–158. <https://doi.org/10.1016/j.oceaneng.2018.07.062>.
- Gong, W., Z. Cai, and D. Liang. 2014. "Adaptive Ranking Mutation Operator Based Differential Evolution for Constrained Optimization." *IEEE Transactions on Cybernetics* 45 (4): 716–727. <https://doi.org/10.1109/TCYB.2014.2334692>.
- Huang, Z., H. Qiu, M. Zhao, X. Cai, and L. Gao. 2015. "An Adaptive SVR-HDMR Model for Approximating High Dimensional Problems." *Engineering Computations* 32 (3): 643–667. <https://doi.org/10.1108/EC-08-2013-0208>.
- Huang, F., L. Wang, and C. Yang. 2016. "A New Improved Artificial Bee Colony Algorithm for Ship Hull Form Optimization." *Engineering Optimization* 48 (4): 672–686. <https://doi.org/10.1080/0305215X.2015.1031660>.
- ITTC, R. 2011. *Procedures and Guidelines: Practical Guidelines for Ship CFD Applications*, 7.5. Boulder, CO: ITTC.
- Jeong, S., and H. Kim. 2013. "Development of an Efficient Hull Form Design Exploration Framework." *Mathematical Problems in Engineering* 2013: 838354. <https://doi.org/10.1155/2013/838354>.
- Ji, L., G. Chen, L. Qian, J. Ma, and J. Tang. 2022. "An Iterative Interval Analysis Method Based on Kriging-HDMR for Uncertainty Problems." *Acta Mechanica Sinica* 38 (7): 521378. <https://doi.org/10.1007/s10409-022-09018-x>.
- Kim, H., C. Yang, S. Jeong, and F. Noblesse. 2011. "Hull Form Design Exploration Based on Response Surface Method." In *ISOPE International Ocean and Polar Engineering Conference, ISOPE-I-11-186*: ISOPE.
- Li, G., X. Xing, W. Welsh, and H. Rabitz. 2017. "High Dimensional Model Representation Constructed by Support Vector Regression. I. Independent Variables with Known Probability Distributions." *Journal of Mathematical Chemistry* 55 (1): 278–303. <https://doi.org/10.1007/s10910-016-0690-z>.
- Li, S., F. Zhu, X. Hou, and Q. Ni. 2022. "Application of Mesh Deformation and Adaptive Method in Hullform Design Optimization." *Journal of Marine Science and Technology* 27: 566–575. <https://doi.org/10.1007/s00773-021-00851-9>.

- Lin, Q., J. Hu, Q. Zhou, Y. Cheng, Z. Hu, I. Couckuyt, and T. Dhaene. 2021. "Multi-output Gaussian Process Prediction for Computationally Expensive Problems with Multiple Levels of Fidelity." *Knowledge-Based Systems* 227: 107151. <https://doi.org/10.1016/j.knosys.2021.107151>
- Liu, H., J.-R. Hervas, Y.-S. Ong, J. Cai, and Y. Wang. 2018. "An Adaptive RBF-HDMR Modeling Approach Under Limited Computational Budget." *Structural Multidisciplinary Optimization* 57 (3): 1233–1250. <https://doi.org/10.1007/s00158-017-1807-0>.
- Luo, X., E. Li, and H. Wang. 2021. "A Surrogate Assisted Thermal Optimization Framework for Design of Pin-Fin Heat Sink for the Platform Inertial Navigation System." *Engineering Optimization* 53 (1): 145–164. <https://doi.org/10.1080/0305215X.2020.1712378>.
- Mahmood, S., and D. Huang. 2012. "Computational Fluid Dynamics Based Bulbous Bow Optimization Using a Genetic Algorithm." *Journal of Marine Science and Application* 11 (3): 286–294. <https://doi.org/10.1007/s11804-012-1134-1>.
- Mallipeddi, R., P. N. Suganthan, Q.-K. Pan, and M. F. Tasgetiren. 2011. "Differential Evolution Algorithm with Ensemble of Parameters and Mutation Strategies." *Applied Soft Computing* 11 (2): 1679–1696. <https://doi.org/10.1016/j.asoc.2010.04.024>.
- Maruo, H., Kasahara K, and Takusagawa Z., et al. 1977. "A Trial of Determining High Speed Practical Hull Forms by the Aid of the Minimum Wave Resistance Theory." *Journal of the Society of Naval Architects of Japan* 1977 (141): 1–9.
- Meng, X.-Y., Y.-L. Hu, Y.-H. Hou, and W.-Q. Wang. 2010. "The Analysis of Chaotic Particle Swarm Optimization and the Application in Preliminary Design of Ship." In *2010 IEEE International conference on mechatronics and automation*, 179–184: IEEE.
- Nazemian, A., and P. Ghadimi. 2021. "CFD-Based Optimization of a Displacement Trimaran Hull for Improving Its Calm Water and Wavy Condition Resistance." *Applied Ocean Research* 113: 102729. <https://doi.org/10.1016/j.apor.2021.102729>.
- Park, D.-W., and H.-H. Chun. 2009. "Design Practice for the Stern Hull Form of a Twin-Skeg Ship." *Journal of Marine Science and Technology* 14 (3): 310–321. <https://doi.org/10.1007/s00773-009-0046-5>.
- Peri, D., M. Rossetti, and E. F. Campana. 2001. "Design Optimization of Ship Hulls via Cfd Techniques." *Journal of Ship Research* 45 (02): 140–149. <https://doi.org/10.5957/jsr.2001.45.2.140>.
- Qin, A. K., V. L. Huang, and P. N. Suganthan. 2008. "Differential Evolution Algorithm with Strategy Adaptation for Global Numerical Optimization." *IEEE Transactions on Evolutionary Computation* 13 (2): 398–417. <https://doi.org/10.1109/TEVC.2008.927706>.
- Rabitz, H., and ÖF Aliş. 1999. "General Foundations of High-Dimensional Model Representations." *Journal of Mathematical Chemistry* 25 (2/3): 197–233. <https://doi.org/10.1023/A:1019188517934>.
- Ren, C., Y. Aoues, D. Lemosse, and E. S. De Cursi. 2022. "Ensemble of Surrogates Combining Kriging and Artificial Neural Networks for Reliability Analysis with Local Goodness Measurement." *Structural Safety* 96:102186. <https://doi.org/10.1016/j.strusafe.2022.102186>.
- Sederberg, T. W., and S. R. Parry. 1986. "Free-Form Deformation of Solid Geometric Models." In *Proceedings of the 13th annual conference on computer graphics and interactive techniques*, 151–160.
- Shan, S., and G. G. Wang. 2009. "Development of Adaptive RBF-HDMR Model for Approximating High Dimensional Problems." In *International design engineering technical conferences and computers and information in engineering conference*, 727–740.
- Simonsen, C. D., J. F. Otzen, S. Joncquez, and F. Stern. 2013. "EFD and CFD for KCS Heaving and Pitching in Regular Head Waves." *Journal of Marine Science and Technology* 18 (4): 435–459. <https://doi.org/10.1007/s00773-013-0219-0>.
- Sobol', I. M. 2003. "Theorems and Examples on High Dimensional Model Representation." *Reliability Engineering and System Safety* 79 (2): 187–193. [https://doi.org/10.1016/S0951-8320\(02\)00229-6](https://doi.org/10.1016/S0951-8320(02)00229-6).
- Thiagarajan, K. P., and E. C. Braddock. 2010. "Influence of Bilge Keel Width on the Roll Damping of FPSO." *ASME. The Journal of Offshore Mechanics and Arctic Engineering* 132 (1): 011303.
- Tian, X., X. Sun, G. Liu, Y. Xie, Y. Chen, and H. Wang. 2021. "Multi-objective Optimization of the Hull Form for the Semi-submersible Medical Platform." *Ocean Engineering* 230: 109038. <https://doi.org/10.1016/j.oceaneng.2021.109038>.
- Veritas, D. N. 2009. "Hull Structural Design, Ships with Length 100 Metres and Above." *DNV Rules for Classification of Ships*.
- Wan, Y., Y. Hou, Y. Xiong, Z. Dong, Y. Zhang, and C. Gong. 2022. "Interval Optimization Design of a Submersible Surface Ship Form Considering the Uncertainty of Surrogate Model." *Ocean Engineering* 263: 112262. <https://doi.org/10.1016/j.oceaneng.2022.112262>.
- Wang, L., F. Huang, C. Yang, and R. Datla. 2015. "Hydrodynamic Optimization of a Wedge Hull." *SNAME international conference on fast sea transportation*, D021S05R01: SNAME.
- Wang, X., L. Parast, L. Han, L. Tian, and T. Cai. 2023. "Robust Approach to Combining Multiple Markers to Improve Surrogacy." *Biometrics* 79 (2): 788–798. <https://doi.org/10.1111/biom.13677>.
- Wang, H., L. Tang, and G. Li. 2011. "Adaptive MLS-HDMR Metamodeling Techniques for High Dimensional Problems." *Expert Systems with Applications* 38 (11): 14117–14126. <https://doi.org/10.1016/j.eswa.2011.04.222>.

- Wang, L., S. Zheng, X. Liu, H. Xie, and J. Dou. 2021. "Flow Resistance Optimization of Link Lever Butterfly Valve Based on Combined Surrogate Model." *Structural and Multidisciplinary Optimization* 64 (6): 4255–4270. <https://doi.org/10.1007/s00158-021-03060-5>.
- Wei, X., H. Chang, B. Feng, and Z. Liu. 2019. "Sensitivity Analysis Based on Polynomial Chaos Expansions and Its Application in Ship Uncertainty-Based Design Optimization." *Mathematical Problems in Engineering* 2019: 7498526. <https://doi.org/10.1155/2019/7498526>.
- Wei, X., H. Chang, B. Feng, Z. Liu, and C. Huang. 2019. "Hull Form Reliability-Based Robust Design Optimization Combining Polynomial Chaos Expansion and Maximum Entropy Method." *Applied Ocean Research* 90: 101860. <https://doi.org/10.1016/j.apor.2019.101860>.
- Zhang, Q., P. Qiao, and Y. Wu. 2024. "A Novel Kriging-Improved High-Dimensional Model Representation Meta-modelling Technique for Approximating High-Dimensional Problems." *Engineering Optimization*, Ahead-of-print: 1–24.
- Zhang, Q., Y. Wu, L. Lu, and P. Qiao. 2022. "An Adaptive Dendrite-HDMR Metamodeling Technique for High-Dimensional Problems." *Journal of Mechanical Design* 144 (8): 081701. <https://doi.org/10.1115/1.4053526>.
- Zhao, H. 2018. "High Dimension Model Representation-Based Response Surface for Reliability Analysis of Tunnel." *Mathematical Problems in Engineering* 2018: 1–10.
- Zhou, H., B. Feng, Z. Liu, H. Chang, and X. Cheng. 2022. "NURBS-Based Parametric Design for Ship Hull Form." *Journal of Marine Science and Engineering* 10 (5): 686. <https://doi.org/10.3390/jmse10050686>.
- Zhou, Q., Y. Wang, P. Jiang, X. Shao, S.-K. Choi, J. Hu, L. Cao, and X. Meng. 2017. "An Active Learning Radial Basis Function Modeling Method Based on Self-Organization Maps for Simulation-Based Design Problems." *Knowledge-Based Systems* 131: 10–27. <https://doi.org/10.1016/j.knsys.2017.05.025>.

Appendix A

The expressions for numerical test cases of different dimensions are shown in Tables A1–A4.

Table A1. 10-dimensional numerical test cases.

No.	Expression	Design space
1	$f(x) = \sum_{i=1}^D (x_i^2 - 10 \cos(2 * \pi i * x_i) + 10)$	$x_i \in [-1, 1]$
2	$f(x) = \sum_{i=1}^D x_i^2 + \left(\frac{1}{2} \sum_{i=1}^D ix_i \right)^2 + \left(\frac{1}{2} \sum_{i=1}^D ix_i \right)^4$	$x_i \in [-10, 10]$
3	$f(x) = \sum_{i=1}^D \{ \ln(x_i - 2) \}^2 + \{ \ln(10 - x_i) \}^2 + \left(\prod_{i=1}^D x_i \right)^{0.2}$	$x_i \in [2.1, 9.9]$
4	$f(x) = \sum_{i=1}^{10} x_i \left(c_i + \ln \frac{x_i}{\sum_{i=1}^{10} x_i} \right)$	$x_i \in [1e^{-6}, 10]$
5	$f(x) = 1 + \sum_{i=1}^D \frac{(x_i - 100)^2}{4000} - \prod_{i=1}^D \cos \left(\frac{(x_i - 100)^2}{4000} \right)$	$x_i \in [-600, 600]$

Note: $c_{1 \leq i \leq 10} = -6.089, -17.164, -34.054, -5.914, -24.721, -14.986, -24.1, -10.708, -26.662, -22.179$.

Appendix B

B.1 10-dimensional results

The bar chart in Figure B1 illustrates the modelling accuracy results for the five 10-dimensional numerical test cases. It can be observed that the modelling accuracy of the PWPV-HDMR model is generally the best, while the kriging model consistently performs the worst in cases 1 and 5. Among the three basic HDMR models, kriging-HDMR performs the best in case 4, PRS-HDMR excels in cases 3 and 5, and SVR-HDMR performs the best in case 1. This indicates that these three models have their strengths and weaknesses, justifying the significance of composing a combined surrogate model.

From the line chart in Figure B1, the following is evident. (1) For cases 1 and 5, where the four error metrics of the three basic HDMR models are significantly better than those of the kriging model, it is logical to conclude that

Table A2. 20-dimensional numerical test cases.

No.	Expression	Design space
6	$f(x) = \sum_{i=1}^D (x_i^2 - 10 \cos(2 * pi * x_i) + 10)$	$x_i \in [-1, 1]$
7	$f(x) = (x_1 - 1)^2 + \sum_{i=2}^{20} i(2x_i^2 - x_{i-1})^2$	$x_i \in [-10, 10]$
8	$f(x) = \sum_{i=1}^D \{\ln(x_i - 2)\}^2 + (\ln(10 - x_i))^2 + \left(\prod_{i=1}^D x_i\right)^{0.2}$	$x_i \in [2.1, 9.9]$
9	$f(x) = \sum_{i=1}^{19} [100(x_{i+1} - x_i^2)^2 + (x_i - 1)^2]$	$x_i \in [-2.1, 2.1]$

Table A3. 30-dimensional numerical test cases.

No.	Expression	Design space
10	$f(x) = \sum_{i=1}^D (x_i^2 - 10 \cos(2 * pi * x_i) + 10)$	$x_i \in [-1, 1]$
11	$f(x) = \sum_{i=1}^D \{\ln(x_i - 2)\}^2 + (\ln(10 - x_i))^2 + \left(\prod_{i=1}^D x_i\right)^{0.2}$	$x_i \in [2.1, 9.9]$
12	$f(x) = 1 + \sum_{i=1}^D \frac{(x_i - 100)^2}{4000} - \prod_{i=1}^D \cos\left(\frac{(x_i - 100)^2}{4000}\right)$	$x_i \in [-600, 600]$

Table A4. 40-dimensional numerical test cases.

No.	Expression	Design space
13	$f(x) = \sum_{i=1}^D (x_i^2 - 10 \cos(2 * pi * x_i) + 10)$	$x_i \in [-1, 1]$
14	$f(x) = \sum_{i=1}^D \{\ln(x_i - 2)\}^2 + (\ln(10 - x_i))^2 + \left(\prod_{i=1}^D x_i\right)^{0.2}$	$x_i \in [2.1, 9.9]$
15	$f(x) = 1 + \sum_{i=1}^D \frac{(x_i - 100)^2}{4000} - \prod_{i=1}^D \cos\left(\frac{(x_i - 100)^2}{4000}\right)$	$x_i \in [-600, 600]$

the PWPV-HDMR model is superior to kriging. (2) For cases 2 and 3, the three basic HDMR models show minimal improvement over the kriging model, and perform worse than the kriging model in the RAAE metric. Consequently, the PWPV-HDMR model exhibits a similar trend. (3) In case 4, both PRS-HDMR and SVR-HDMR models perform worse than the kriging model, but the PWPV-HDMR model clearly learns the characteristics of kriging-HDMR, achieving better results than kriging in terms of RRMSE and RAAE metrics.

B.2 20-dimensional results

The bar chart in Figure B2 illustrates the modelling accuracy results for the four 20-dimensional numerical test cases. It can be observed that the results of the PWPV-HDMR model are consistently the closest or directly the best, while the results of the kriging model are mostly the worst. Among the three basic HDMR models, kriging-HDMR performs the best in case 7, PRS-HDMR excels in cases 8 and 9, and SVR-HDMR performs the best in case 6, with PRS-HDMR having a slightly better overall performance.

From the line chart in Figure B2, the following is evident. (1) In cases 6, 7 and 8, the PWPV-HDMR model is the best. (2) In case 9, the PRS-HDMR model is the best, but the gap between the PRS-HDMR and PWPV-HDMR models is minimal. This indicates that the PWPV-HDMR model has the ability to learn from the best-performing basic HDMR models, but may not always surpass them.

Table B1. Comparative results of the modelling accuracy (10 dimensions).

Function	Surrogates	R^2	RRMSE	RMAE	RAAE	NOP
1	PWPV-HDMR	9.99E-01	2.36E-02	7.87E-02	1.89E-02	81 + 47
	Kriging-HDMR	9.95E-01	7.14E-02	2.41E-01	5.78E-02	
	PRS-HDMR	9.07E-01	3.06E-01	9.58E-01	2.49E-01	
	SVR-HDMR	9.99E-01	2.35E-02	8.03E-02	1.88E-02	
	Kriging	<i>-5.14E-01</i>	<i>1.23E+00</i>	<i>3.36E+00</i>	<i>1.01E+00</i>	
2	PWPV-HDMR	5.37E-01	6.80E-01	8.93E+00	2.97E-01	61 + 182
	Kriging-HDMR	4.88E-01	7.16E-01	9.20E+00	3.32E-01	
	PRS-HDMR	4.54E-01	7.39E-01	9.11E+00	<i>4.04E-01</i>	
	SVR-HDMR	<i>3.26E-01</i>	<i>8.21E-01</i>	<i>9.97E+00</i>	2.71E-01	
	Kriging	4.38E-01	7.49E-01	9.71E+00	2.25E-01	
3	PWPV-HDMR	9.42E-01	2.41E-01	8.96E-01	1.86E-01	81 + 182
	Kriging-HDMR	9.26E-01	2.73E-01	1.43E+00	2.11E-01	
	PRS-HDMR	9.32E-01	2.60E-01	8.13E-01	2.15E-01	
	SVR-HDMR	<i>8.50E-01</i>	<i>3.88E-01</i>	1.24E+00	<i>3.15E-01</i>	
	Kriging	9.09E-01	3.02E-01	<i>1.87E+00</i>	2.29E-01	
4	PWPV-HDMR	9.99E-01	6.13E-03	4.14E-02	3.62E-03	41 + 2
	Kriging-HDMR	9.99E-01	8.33E-03	4.92E-02	5.03E-03	
	PRS-HDMR	<i>9.40E-01</i>	<i>2.45E-01</i>	<i>9.67E-01</i>	<i>1.96E-01</i>	
	SVR-HDMR	9.94E-01	7.95E-02	2.95E-01	6.34E-02	
	Kriging	9.99E-01	1.29E-02	4.05E-02	1.07E-02	
5	PWPV-HDMR	9.99E-01	2.42E-02	4.93E-02	2.29E-02	51 + 2
	Kriging-HDMR	9.99E-01	2.43E-02	4.93E-02	2.30E-02	
	PRS-HDMR	9.99E-01	3.02E-02	6.36E-02	2.86E-02	
	SVR-HDMR	9.85E-01	1.23E-01	3.78E-01	1.06E-01	
	Kriging	<i>2.31E-01</i>	<i>8.75E-01</i>	<i>2.72E+00</i>	<i>6.87E-01</i>	

Note: Best results are shown in bold; worst results in italic.

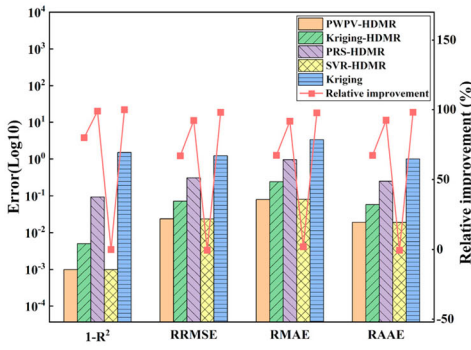
PWPV-HDMR = pointwise weighting prediction variance–high-dimensional model representation; HDMR = high-dimensional model representation; PRS = polynomial response surface; SVR = support vector regression; R^2 = coefficient of determination; RRMSE = relative root mean square error; RMAE = relative maximum absolute error; RAAE = relative average absolute error; NOP = number of sample points.

Table B2. Comparative results of the modelling accuracy (20 dimensions).

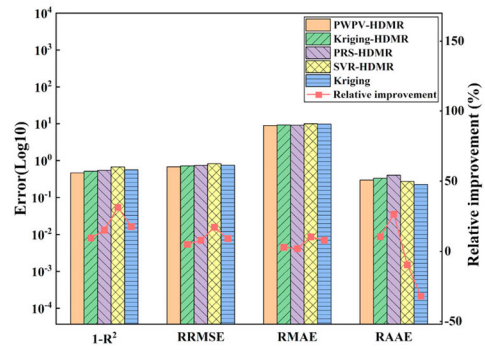
Function	Surrogate	R^2	RRMSE	RMAE	RAAE	NOP
6	PWPV-HDMR	9.98E-01	4.90E-02	1.34E-01	4.04E-02	141 + 2
	Kriging-HDMR	9.75E-01	1.58E-01	3.94E-01	1.36E-01	
	PRS-HDMR	7.20E-01	5.27E-01	1.28E+00	4.69E-01	
	SVR-HDMR	9.97E-01	5.25E-02	1.29E-01	4.53E-02	
	Kriging	<i>-3.72E+01</i>	<i>6.18E+00</i>	<i>9.17E+00</i>	<i>6.09E+00</i>	
7	PWPV-HDMR	9.54E-01	2.15E-01	6.45E-01	1.72E-01	161 + 249
	Kriging-HDMR	9.40E-01	2.45E-01	8.21E-01	2.07E-01	
	PRS-HDMR	8.95E-01	3.23E-01	1.28E+00	2.55E-01	
	SVR-HDMR	8.70E-01	3.60E-01	1.42E+00	2.85E-01	
	Kriging	<i>8.24E-01</i>	<i>4.19E-01</i>	<i>1.70E+00</i>	<i>3.32E-01</i>	
8	PWPV-HDMR	9.74E-01	1.62E-01	1.26E+00	8.58E-02	121 + 762
	Kriging-HDMR	9.63E-01	1.91E-01	1.45E+00	1.02E-01	
	PRS-HDMR	9.71E-01	1.70E-01	1.29E+00	1.07E-01	
	SVR-HDMR	<i>8.91E-01</i>	<i>3.30E-01</i>	<i>1.69E+00</i>	<i>2.66E-01</i>	
	Kriging	9.20E-01	2.82E-01	1.29E+00	2.09E-01	
9	PWPV-HDMR	1.00E+00	9.69E-16	3.30E-15	7.47E-16	141 + 762
	Kriging-HDMR	9.89E-01	1.07E-01	3.02E-01	8.64E-02	
	PRS-HDMR	1.00E+00	9.68E-16	3.29E-15	7.46E-16	
	SVR-HDMR	8.66E-01	3.64E-01	1.05E+00	2.94E-01	
	Kriging	<i>1.72E-01</i>	<i>9.10E-01</i>	<i>4.86E+00</i>	<i>7.01E-01</i>	

Note: Best results are shown in bold; worst results in italic.

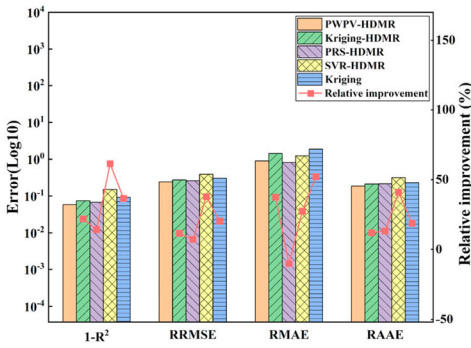
PWPV-HDMR = pointwise weighting prediction variance–high-dimensional model representation; HDMR = high-dimensional model representation; PRS = polynomial response surface; SVR = support vector regression; R^2 = coefficient of determination; RRMSE = relative root mean square error; RMAE = relative maximum absolute error; RAAE = relative average absolute error; NOP = number of sample points.



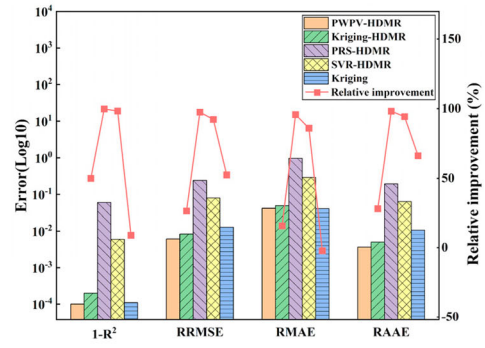
(a) function No.1



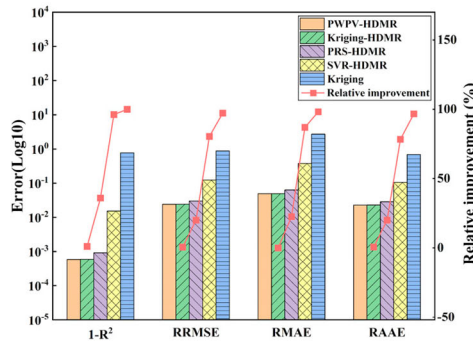
(b) function No.2



(c) function No.3

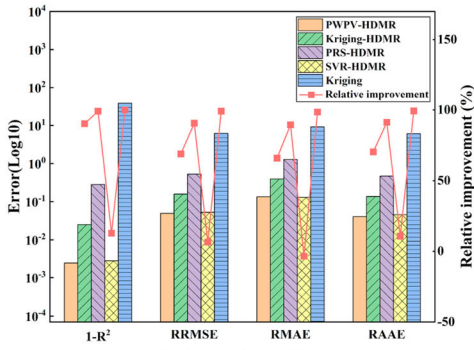


(d) function No.4

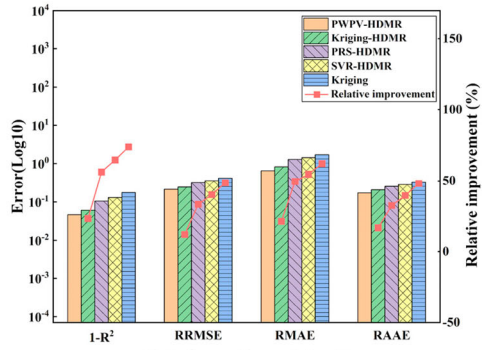


(e) function No.5

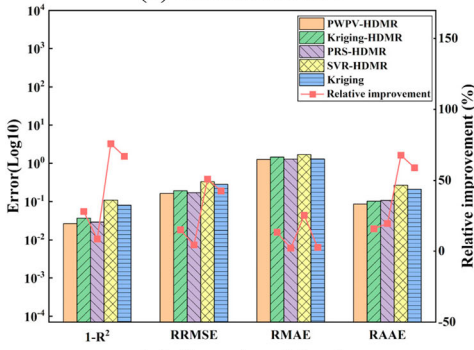
Figure B1. Modelling accuracy and relative improvement of pointwise weighting prediction variance–high-dimensional model representation (PWPV-HDMR) (10 dimensions): (a) function no. 1; (b) function no. 2; (c) function no. 3; (d) function no. 4; (e) function no. 5. HDMR = high-dimensional model representation; PRS = polynomial response surface; SVR = support vector regression; R^2 = coefficient of determination; RRMSE = relative root mean square error; RMAE = relative maximum absolute error; RAAE = relative average absolute error.



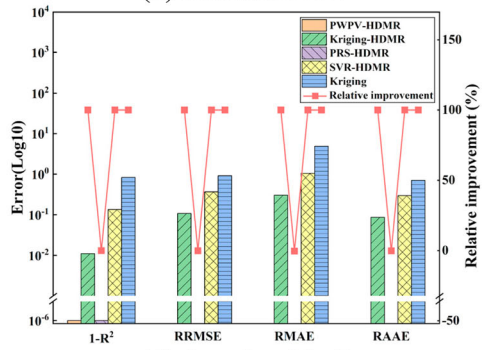
(a) function No.6



(b) function No.7



(c) function No.8



(d) function No.9

Figure B2. Modelling accuracy and relative improvement of pointwise weighting prediction variance–high-dimensional model representation (PWPV-HDMR) (20 dimensions): (a) function no. 6; (b) function no. 7; (c) function no. 8; (d) function no. 9. HDMR = high-dimensional model representation; PRS = polynomial response surface; SVR = support vector regression; R^2 = coefficient of determination; RRMSE = relative root mean square error; RMAE = relative maximum absolute error; RAAE = relative average absolute error.